arXiv:1412.6993v2 [cond-mat.mtrl-sci] 19 Apr 2015

Theory of anharmonic phonons in 2D crystals

K. H. Michel,[1,*] S. Costamagna,[2,1,†] and F. M. Peeters[1,‡]

[1] *Universiteit Antwerpen, Department of Physics, Groenenborgerlaan 171, BE-2020 Antwerpen, Belgium.*

[2] *Instituto de Física Rosario, Bv. 27 de Febrero 210 bis, 2000 Rosario, Argentina.*

(Dated: April 21, 2015)

Anharmonic effects in an atomic monolayer thin crystal with honeycomb lattice structure are investigated by analytical and numerical lattice dynamical methods. Starting from a semi-empirical model for anharmonic couplings of third and fourth order, we study the in-plane and out-of-plane (flexural) mode components of the generalized wave vector dependent Grüneisen parameters, the thermal tension and the thermal expansion coefficients as function of temperature and crystal size. From the resonances of the displacement-displacement correlation functions we obtain the renormalization and decay rate of in-plane and flexural phonons as function of temperature, wave vector and crystal size in the classical and in the quantum regime. Quantitative results are presented for graphene. There we find that the transition temperature T_α from negative to positive thermal expansion is lowered with smaller system size. Renormalization of the flexural mode has the opposite effect and leads to values of $T_\alpha \approx$300 K for systems of macroscopic size. Extensive numerical analysis throughout the Brillouin zone explores various decay and scattering channels. The relative importance of Normal and Umklapp processes is investigated. The work is complementary to crystalline membrane theory and computational studies of anharmonic effects in two-dimensional crystals.

PACS numbers:

I. INTRODUCTION

Phonon-phonon interactions due to the anharmonicity of lattice forces are essential for the understanding of thermoelastic properties and heat transport in solids[1]. While for three-dimensional (3D) crystals the subject is well established[2], the discovery of graphene and of other two-dimensional(2D) crystals[3–5] has given new impetus to experimental and theoretical studies of anharmonicity related phenomena in ultra-thin crystals with a countable number of layers.

Electron microscopy and diffraction studies have proven the existence of ripples in single- and bi-layer graphene membranes[6]. The thermal expansion of graphene has been found to be negative[7] in the measured temperature range between 200-400 K while earlier experiments[8] had led to the estimate that a transition to positive values occurs near 350 K. Measurements of thermal conductivity $\varkappa$ on suspended single-layer graphene revealed an anomalous large value above the in-plane bulk graphite value[9]. Since then the determination of $\varkappa$ as function of temperature T in suspended and in supported[10] single- and few-layer graphene[11] is an important topic of experimental and theoretical research[12].

Theoretical explanations of all these phenomena are related to the anharmonic coupling between in-plane stretching and out-of-plane bending or flexural phonon modes. Such a coupling was originally suggested[13] as a membrane effect and explains the negative coefficient of thermal expansion in layered structures. Ab-initio density functional theory (DFT) calculations[14] show that the thermal contraction in graphene subsists up to $T > 2000$ K. Atomistic Monte Carlo simulations[15] exhibit a crossover from contraction to expansion near 900 K. Most recently the thermal expansion in monolayer graphene has been calculated by the unsymmetrized self consistent field method[16]. Monte Carlo simulations also suggest that the formation of ripples[6] due to anharmonic coupling leads to the stabilization of graphene as a 2D crystal[17]. Acoustic phonon lifetimes in free standing and in strained graphene have been calculated by DFT methods[18,19] and the results have been used to estimate the T dependence of the intrinsic anharmonic thermal conductivity[19]. Recent analytic studies[20] of thermodynamic properties by continuum field theory methods exploit the equivalence[21] between graphene treated in the continuum approximation and a crystalline (polymerized) membrane[22]. Within the continuum theory of thin sheets[21,23] the in-plane strains comprise terms which are quadratic in the out-of-plane fluctuations. These terms then lead to anharmonic couplings in the elastic free energy. The resulting phonon mediated interactions between Gaussian curvatures increase the bending rigidity and stabilize the membrane[24].

In the present paper we start from a somewhat different approach based on a discrete atomistic model of a monolayer crystal. We consider a Hamiltonian where the potential energy has been expanded up to fourth order in the atomic displacements. The harmonic and anharmonic coupling coefficients are determined by means of empirical data of phonon dispersions[25] and Grüneisen parameters[26]. As an advantage of such a concept we consider the fact that we can use to a large extent well established analytical and numerical methods from lattice dynamics and at the same time take into account the specific structural properties of a 2D hexagonal crystal.

We will restrict ourselves to the study of thermal ten-

sion (equivalently thermal expansion) and of phonon resonances (shifts and linewidths). Although the thermal conductivity is from the technological point of view the more important quantity, a comprehensive study is beyond the scope of the present work. For an outline of different theoretical approaches developed so far for phonon transport in graphene, see Refs. 27–30.

The content of the paper is as follows. In Section II we recall some basic concepts and definitions of the theory of lattice dynamics and anharmonic phonons. Next, in Sect. III, we first express the thermal tension in terms of phonon related quantities such as vibrational energy and generalized Grüneisen coefficients. We distinguish in-plane and out-of-plane acoustic modes. Secondly we study the resonances of the corresponding displacement-displacement Green's functions, thereby paving the way for a later discussion of phonon linewidths and bandshifts. In Sect. IV we describe a central force constants model which will be used for quantitative calculations. In Sect. V, we present detailed analytical calculations of the generalized Grüneisen coefficients and of the thermal expansion. The competing interplay of out-of-plane modes which favor thermal contraction and of in-plane modes which favor thermal expansion is investigated as function of temperature and crystal size. In Sect. VI we study lineshifts and decay rates of in-plane and out-of-plane modes and the effect of flexural mode renormalization on thermal expansion. In Sect. VII we present extensive numerical calculations of Grüneisen coefficients, thermal expansion, phonon lineshift and decay rates. Concluding remarks (Sect. VIII) close the paper.

II. BASIC CONCEPTS

We recall some elements of lattice dynamics of a non-primitive non-ionic crystal[2,31] and apply these concepts to 2D graphene[32,33].

The crystal consists of N unit cells, each unit cell contains two C atoms which we label by an index κ=1, 2. The positions of the unit cells are fixed by the lattice vectors

$$\vec{X}(\vec{n}) = n_1\vec{a}_1 + n_1\vec{a}_2. \tag{1}$$

Here $\vec{a}_\alpha$ α=1, 2 are two noncolinear basis vectors while $\vec{n}$=(n_1, n_2), where n_i are integers, labels the unit cells. The equilibrium positions of the atoms in the lattice plane are given by

$$\vec{X}(\vec{n}\kappa) = \vec{X}(\vec{n}) + \vec{r}(\kappa), \tag{2}$$

where $\vec{r}(\kappa)$ specifies the positions of the κ-th atom in the $\vec{n}$-th unit cell. We use $u_i(\vec{n}\kappa)$ for the i-th Cartesian components (i=x, y, z) of the instantaneous displacement vector of atom $(\vec{n}\kappa)$ away from its equilibrium position, the z-component refers to the out-of-plane displacements.

The crystal potential energy Φ is a function of the instantaneous positions $\vec{R}(\vec{n}\kappa)$=$\vec{X}(\vec{n}\kappa)$ + $\vec{u}(\vec{n}\kappa)$ of the atoms. Expansion of the potential energy in terms of displacements away from the equilibrium position gives

$$\Phi = \Phi^{(0)} + \Phi^{(2)} + \Phi^{(3)} + \Phi^{(4)} + ... \quad . \tag{3}$$

Here $\Phi^{(0)}$ is the rigid lattice potential, $\Phi^{(2)}$ the harmonic potential and $\Phi^{(3)}$, $\Phi^{(4)}$ are the third order and fourth order anharmonic potential contributions. Explicitly we write

$$\Phi^{(2)} = \frac{1}{2}\sum_{\vec{n}\kappa}\sum_{\vec{n}'\kappa'}\sum_{ij}\Phi^{(2)}_{ij}(\vec{n}\kappa;\vec{n}'\kappa')u_i(\vec{n}\kappa)u_j(\vec{n}'\kappa') \tag{4a}$$

$$\Phi^{(3)} = \frac{1}{3!}\sum_{\vec{n}\kappa}\sum_{\vec{n}'\kappa'}\sum_{\vec{n}''\kappa''}\sum_{ijk}\Phi^{(3)}_{ijk}(\vec{n}\kappa;\vec{n}'\kappa';\vec{n}''\kappa'') \times u_i(\vec{n}\kappa)u_j(\vec{n}'\kappa')u_k(\vec{n}''\kappa'') \tag{4b}$$

$$\Phi^{(4)} = \frac{1}{4!}\sum_{\vec{n}\kappa}\sum_{\vec{n}'\kappa'}\sum_{\vec{n}''\kappa''}\sum_{\vec{n}'''\kappa'''}\sum_{ijkl}\Phi^{(4)}_{ijkl}(\vec{n}\kappa;\vec{n}'\kappa';\vec{n}''\kappa'';\vec{n}'''\kappa''') \times u_i(\vec{n}\kappa)u_j(\vec{n}'\kappa')u_k(\vec{n}''\kappa'')u_l(\vec{n}'''\kappa''') \tag{4c}$$

The coupling parameters $\Phi^{(2)}_{ij}(\vec{n}\kappa;\vec{n}'\kappa')$, $\Phi^{(3)}_{ijk}(\vec{n}\kappa;\vec{n}'\kappa';\vec{n}''\kappa'')$ and $\Phi^{(4)}_{ijkl}(\vec{n}\kappa;\vec{n}'\kappa';\vec{n}''\kappa'';\vec{n}'''\kappa''')$ are the second, third and fourth order derivatives of the potential energy with respect to the displacements, taken at the equilibrium positions.

The kinetic energy of the crystal is given by

$$T = \sum_{\vec{n}\kappa}\sum_{i}\frac{p_i^2(\vec{n}\kappa)}{2M_\kappa}, \tag{5}$$

where $p_i(\vec{n}\kappa)$ are the components of the momentum conjugate to $u_i(\vec{n}\kappa)$ and where M_κ is the mass of the κ-th atom. In case of graphene with two C atoms per unit cell one has M_1=M_2=M_C where M_C=12 au is the mass

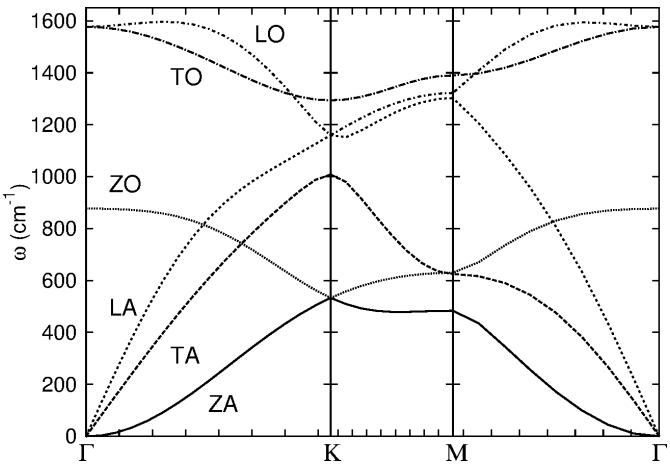

FIG. 1: Phonon modes of graphene along the high symmetry crystallographic direction ΓK-MΓ (Ref. 35).

of the carbon atom. The area of the unit cell is given by $v_{2D} = a^2\sqrt{3}/2$, with $|\vec{a}_1| = |\vec{a}_2| = a = 2.46\mathring{A}$.

In the following we restrict ourselves to lowest order anharmonicities and consider $\Phi^{(3)}$ and $\Phi^{(4)}$ as a perturbations to the harmonic Hamiltonian H_h=$(T+\Phi^{(2)})$. We introduce Fourier transforms in space and time by writing

$$u_i(\vec{n}\kappa) = \frac{1}{\sqrt{M_C N}} \sum_{\vec{q}} u_i^{\kappa}(\vec{q}) e^{i\vec{q}\cdot\vec{X}(\vec{n}\kappa) - i\omega t} \tag{6}$$

Here $\vec{q}$ is the wave vector in the 2D Brillouin zone (BZ) while ω is the frequency. The 6×6 dynamical matrix $D(\vec{q})$ has the elements:

$$D_{ij}^{\kappa\kappa'}(\vec{q}) = \frac{1}{M_C} \sum_{\vec{n}'} \Phi_{ij}^{(2)}(\vec{n}\kappa; \vec{n}'\kappa') e^{i\vec{q}\cdot[\vec{X}(\vec{n}'\kappa') - \vec{X}(\vec{n}\kappa)]} \tag{7}$$

and is Hermitian. Solving the secular equation one obtains the eigenfrequencies $\omega(\vec{q},\lambda)$, $\lambda = 1, ..., 6$, and the eigenvectors $\vec{e}(\vec{q},\lambda)$ with components $e_i^{\kappa}(\vec{q},\lambda)$, κ=1, 2 and i=x, y, z. As is well known[32] there are three acoustical branches which we label by ZA, TA and LA and three optical branches which we label by ZO, TO and LO (See Fig. 1).

In terms of phonon annihilation and creation operators $b_{\vec{q}}^{\lambda}$ and $b_{-\vec{q}}^{\lambda\dagger}$, that satisfy the usual commutation relations for Bose operators, the harmonic part of the Hamiltonian reads

$$H_h = \sum_{\vec{q}} \sum_{\lambda} \hbar\omega(\vec{q},\lambda) \left(b_{\vec{q}}^{\lambda\dagger} b_{\vec{q}}^{\lambda} + \frac{1}{2} \right). \tag{8}$$

With $B\left(\begin{smallmatrix}\lambda\\ \vec{q}\end{smallmatrix}\right) = \left(b_{\vec{q}}^{\lambda} + b_{-\vec{q}}^{\lambda\dagger}\right)$. The third order anharmonic contribution in Eq. (3) is given by

$$\Phi^{(3)} = \frac{\hbar^{3/2}}{3! N^{1/2}} \sum_{\vec{q}_1\vec{q}_2\vec{q}_3} \sum_{\lambda_1\lambda_2\lambda_3} \Phi^{(3)}\begin{pmatrix}\lambda_1\lambda_2\lambda_3\\ \vec{q}_1\vec{q}_2\vec{q}_3\end{pmatrix} B\begin{pmatrix}\lambda_1\\ \vec{q}_1\end{pmatrix} B\begin{pmatrix}\lambda_2\\ \vec{q}_2\end{pmatrix} B\begin{pmatrix}\lambda_3\\ \vec{q}_3\end{pmatrix}, \tag{9}$$

with

$$\Phi^{(3)}\begin{pmatrix}\lambda_1\lambda_2\lambda_3\\ \vec{q}_1\vec{q}_2\vec{q}_3\end{pmatrix} = \sum_{\kappa_1 i} \sum_{\kappa_2 j} \sum_{\kappa_3 k} \frac{e_i^{\kappa_1}(\vec{q}_1,\lambda_1) e_j^{\kappa_2}(\vec{q}_2,\lambda_2) e_k^{\kappa_3}(\vec{q}_3,\lambda_3)}{\sqrt{8\omega(\vec{q}_1,\lambda_1)\omega(\vec{q}_2,\lambda_2)\omega(\vec{q}_3,\lambda_3)}} \Phi_{ijk}^{(3)}\begin{pmatrix}\kappa_1\kappa_2\kappa_3\\ \vec{q}_1\vec{q}_2\vec{q}_3\end{pmatrix}. \tag{10}$$

Invariance of the crystal by a displacement through a lattice translation vector implies that

$$\begin{aligned}\Phi_{ijk}^{(3)}\begin{pmatrix}\kappa_1\kappa_2\kappa_3\\ \vec{q}_1\vec{q}_2\vec{q}_3\end{pmatrix} =& \frac{1}{\sqrt{M_C^3}} \sum_{\vec{n}_1\vec{n}_2} \Phi_{ijk}^{(3)}(\vec{n}_1\kappa_1; \vec{n}_2\kappa_2; \vec{0}\kappa_3) \\ & \times e^{i[\vec{q}_1\cdot\vec{X}(\vec{n}_1\kappa_1) + \vec{q}_2\cdot\vec{X}(\vec{n}_2\kappa_2) + \vec{q}_3\cdot\vec{r}(\kappa_3)]} \times \Delta(\vec{q}_1 + \vec{q}_2 + \vec{q}_3),\end{aligned} \tag{11}$$

where

$$\Delta(\vec{q}_1 + \vec{q}_2 + \vec{q}_3) = \sum_{\vec{G}} \delta_{\vec{q}_1+\vec{q}_2+\vec{q}_3,\vec{G}}. \tag{12}$$

Here Δ vanishes unless $(\vec{q}_1 + \vec{q}_2 + \vec{q}_3)$ is equal to a lattice vector $\vec{G}$ in 2D reciprocal space. In the latter case Δ=1.

A phonon scattering process with $\vec{G} = 0$ is called Normal while when a non-zero $\vec{G}$ is needed to bring back the scattered phonon inside the first BZ the process is called Umklapp[34].

The fourth order anharmonic term reads

$$\Phi^{(4)} = \frac{\hbar^2}{4! N} \sum_{\vec{q}_1\vec{q}_2\vec{q}_3\vec{q}_4} \sum_{\lambda_1\lambda_2\lambda_3\lambda_4} \Phi^{(4)}\begin{pmatrix}\lambda_1\lambda_2\lambda_3\lambda_4\\ \vec{q}_1\vec{q}_2\vec{q}_3\vec{q}_4\end{pmatrix} B\begin{pmatrix}\lambda_1\\ \vec{q}_1\end{pmatrix} B\begin{pmatrix}\lambda_2\\ \vec{q}_2\end{pmatrix} B\begin{pmatrix}\lambda_3\\ \vec{q}_3\end{pmatrix} B\begin{pmatrix}\lambda_4\\ \vec{q}_4\end{pmatrix}, \tag{13}$$

with

$$\Phi^{(4)}\begin{pmatrix}\lambda_1\lambda_2\lambda_3\lambda_4\\ \vec{q}_1\vec{q}_2\vec{q}_3\vec{q}_4\end{pmatrix} = \sum_{\kappa_1 i} \sum_{\kappa_2 j} \sum_{\kappa_3 k} \sum_{\kappa_4 l} \frac{e_i^{\kappa_1}(\vec{q}_1,\lambda_1) e_j^{\kappa_2}(\vec{q}_2,\lambda_2) e_k^{\kappa_3}(\vec{q}_3,\lambda_3) e_l^{\kappa_4}(\vec{q}_4,\lambda_4)}{\sqrt{16\omega(\vec{q}_1,\lambda_1)\omega(\vec{q}_2,\lambda_2)\omega(\vec{q}_3,\lambda_3)\omega(\vec{q}_3,\lambda_3)}} \Phi_{ijkl}^{(4)}\begin{pmatrix}\kappa_1\kappa_2\kappa_3\kappa_4\\ \vec{q}_1\vec{q}_2\vec{q}_3\vec{q}_4\end{pmatrix}, \tag{14}$$

where

$$\Phi^{(4)}_{ijkl}\begin{pmatrix}\kappa_1\kappa_2\kappa_3\kappa_4\\ \vec{q}_1\vec{q}_2\vec{q}_3\vec{q}_4\end{pmatrix} = \frac{1}{M_C^2}\sum_{\vec{n}_1\vec{n}_2\vec{n}_3}\Phi^{(4)}_{ijkl}(\vec{n}_1\kappa_1;\vec{n}_2\kappa_2;\vec{n}_3\kappa_3;\vec{0}\kappa_4)$$
$$\times e^{i[\vec{q}_1\cdot\vec{X}(\vec{n}_1\kappa_1)+\vec{q}_2\cdot\vec{X}(\vec{n}_2\kappa_2)+\vec{q}_3\cdot\vec{X}(\vec{n}_3\kappa_3)+\vec{q}_4\cdot\vec{r}(\kappa_4)]}\times\Delta(\vec{q}_1+\vec{q}_2+\vec{q}_3+\vec{q}_4). \quad (15)$$

Invariance of the potential energy against infinitesimal translations of the crystal implies for $\nu \geq 2, 3, ...$

$$\sum_{\kappa_1\vec{n}_1}\Phi^{(\nu)}_{ij..}(\vec{n}_1\kappa_1,\vec{n}_2\kappa_2,...,\vec{n}_\nu\kappa_\nu) = 0. \quad (16)$$

III. PHYSICAL QUANTITIES

For the study of thermal expansion and phonon renormalization effects we restrict ourselves to acoustic modes LA, TA and ZA which we denote by L, T and Z. In the long wavelength regime the in-plane mode frequencies read $\omega(\vec{q},\lambda) = c_\lambda q$, where for $\lambda \in \{\mathrm{L},\ \mathrm{T}\}$, c_L and c_T are the longitudinal and transverse sound velocities, respectively. The out-of-plane mode (also called flexural mode) has frequency $\omega(\vec{q},\mathrm{Z}) = \sqrt{\kappa_0}q^2$, where $\kappa_0 = \kappa_B/\rho_{2D}$, κ_B is the bending rigidity coefficient and ρ_{2D} the density. With the harmonic force constant model[35] for graphene we obtain $\kappa_0 = 42.48\times10^{-6}$ cm^4 s^{-2}, which corresponds to $\kappa_B = 3.23\times10^{-12}$ erg ≈ 2.01 eV. Due to a numerical error the value 1.12 eV quoted in Ref. 35 is wrong. One finds a broad range of values for κ_B for graphene in the literature (units eV): 1.68 (Ref. 36), 1.1 (Ref. 20). From out of plane phonon dispersions measured by neutron scattering on graphite[37] we estimate κ_B =2.4 eV.

A. Thermoelastic Phenomena

We want to calculate thermodynamic quantities such as thermal tension and thermal expansion which depend on lattice anharmonicities. We start from an undeformed graphene crystal at an initial temperature T and in the absence of external forces. We recall that the elastic properties of the 2D hexagonal crystal reflect the symmetry of an isotropic solid. A small temperature change will cause isotropic lattice deformations which are described by the thermal expansion coefficient $\alpha_T = \sum_i d\epsilon_{ii}/dT$. Here the strain $\sum_i \epsilon_{ii} \equiv \epsilon_{xx}+\epsilon_{yy}$ characterizes the change of the unit cell area. The thermal expansion is related to the thermal tension β_T by

$$\alpha_T = \beta_T B_{2D}^{-1}. \quad (17)$$

Here B_{2D}=$\lambda_{2D} + \mu_{2D}$ is the bulk modulus, $\lambda_{2D} = \gamma_{12}$ and $\mu_{2D} = \gamma_{66}$ are the elastic tension coefficients[35]. For graphene we use B_{2D}=24.89×10^4 dyn/cm.

Starting from the vibrational energy per unit cell in the quasi-harmonic approximation[38], one obtains the tension coefficient as

$$\beta_T = \frac{1}{v_{2D}N}\sum_{\vec{q}\lambda}\gamma(\vec{q},\lambda)\frac{\partial E(\omega(\vec{q},\lambda),T)}{\partial T}. \quad (18)$$

Here

$$E(\omega(\vec{q},\lambda),T) = \hbar\omega(\vec{q},\lambda)\left[n(\vec{q},\lambda)+\frac{1}{2}\right], \quad (19)$$

is the vibrational energy of phonons with harmonic frequency $\omega(\vec{q},\lambda)$ and $n(\vec{q},\lambda) = (e^{\hbar\omega(\vec{q},\lambda)/k_BT}-1)^{-1}$ is the phonon thermal density at temperature T. The generalized Grüneisen coefficient reads

$$\gamma(\vec{q},\lambda) = -\frac{1}{\omega(\vec{q},\lambda)}\sum_i\frac{\partial\omega(\vec{q},\lambda)}{\partial\epsilon_{ii}}, \quad (20)$$

where $\lambda \in \{\mathrm{T,L,Z}\}$ characterize the relative changes of the acoustic phonon frequencies by strains.

The evaluation of the Grüneisen coefficient requires the calculation of $\partial\omega(\vec{q},\lambda)/\partial\epsilon_{ii}$ which involves anharmonic interactions. Details of the calculation are given in Appendix A and the results are discussed in Sect. V.

B. Phonon Resonances

The anharmonic potentials $\Phi^{(3)}$ and $\Phi^{(4)}$ change the harmonic phonon frequencies $\omega(\vec{q},\lambda)$. We study the resonances of the frequency dependent displacement-displacement Green's function $D(\vec{q},\lambda;z)$.

One derives the Dyson equation[39]

$$[z^2-\omega^2(\vec{q},\lambda)-\Sigma(\vec{q},\lambda;z)]D(\vec{q},\lambda;z) = \hbar, \quad (21)$$

where $z = \omega+i\epsilon$, $\epsilon\to0^+$, is the frequency. The self-energy $\Sigma(\vec{q},\lambda;z)$ reads[39]

$$\Sigma(\vec{q},\lambda;z) = \Sigma'(\vec{q},\lambda;\omega)+i\Sigma''(\vec{q},\lambda;\omega) \quad (22)$$

where

$$\Sigma'(\vec{q},\lambda;\omega) = \Sigma^{(3)'}(\vec{q},\lambda;\omega)+\Sigma^{(4)}(\vec{q},\lambda), \quad (23)$$

with

$$\Sigma^{(3)'}(\vec{q},\lambda;\omega) = \frac{\hbar\omega(\vec{q},\lambda)}{N} P \sum_{\vec{q}_2\vec{q}_3}\sum_{\lambda_2\lambda_3}\left|\Phi^{(3)}\begin{pmatrix}\lambda\lambda_2\lambda_3\\ -\vec{q}\vec{q}_2\vec{q}_3\end{pmatrix}\right|^2 \times\left\{\frac{1+n(\vec{q}_2,\lambda_2)+n(\vec{q}_3,\lambda_3)}{\omega-\omega(\vec{q}_2,\lambda_2)-\omega(\vec{q}_3,\lambda_3)} - \frac{1+n(\vec{q}_2,\lambda_2)+n(\vec{q}_3,\lambda_3)}{\omega+\omega(\vec{q}_2,\lambda_2)+\omega(\vec{q}_3,\lambda_3)} + \frac{2[n(\vec{q}_2,\lambda_2)-n(\vec{q}_3,\lambda_3)]}{\omega+\omega(\vec{q}_2,\lambda_2)-\omega(\vec{q}_3,\lambda_3)}\right\}, \tag{24}$$

with P standing for the principal part,

$$\Sigma^{(4)}(\vec{q},\lambda) = \frac{\hbar\omega(\vec{q},\lambda)}{N}\sum_{\vec{q}_1\lambda_1}\Phi^{(4)}\begin{pmatrix}\lambda\lambda_1\lambda_1\lambda\\ -\vec{q}\vec{q}_1-\vec{q}_1\vec{q}\end{pmatrix}\Big[1+2n(\vec{q}_1,\lambda_1)\Big], \tag{25}$$

and where

$$\Sigma''(\vec{q},\lambda;\omega) = -\frac{\pi\hbar\omega(\vec{q},\lambda)}{N}\sum_{\vec{q}_2\vec{q}_3}\sum_{\lambda_2\lambda_3}\left|\Phi^{(3)}\begin{pmatrix}\lambda\lambda_2\lambda_3\\ -\vec{q}\vec{q}_2\vec{q}_3\end{pmatrix}\right|^2 \times\Big\{\Big[1+n(\vec{q}_2,\lambda_2)+n(\vec{q}_3,\lambda_3)\Big] \Big[\delta\big(\omega-\omega(\vec{q}_2,\lambda_2)-\omega(\vec{q}_3,\lambda_3)\big)-\delta\big(\omega+\omega(\vec{q}_2,\lambda_2)+\omega(\vec{q}_3,\lambda_3)\big)\Big] + 2\Big[n(\vec{q}_2,\lambda_2)-n(\vec{q}_3,\lambda_3)\Big]\delta\big(\omega+\omega(\vec{q}_2,\lambda_2)-\omega(\vec{q}_3,\lambda_3)\big)\Big\}. \tag{26}$$

Within lowest order perturbation theory $\Sigma^{(4)}(\vec{q},\lambda)$ is real. In expressions (24)-(26) the summations in $\vec{q}$-space run over the 2D Brillouin zone.

The resonances of $D(\vec{q},\lambda,z)$ near ω=$\omega(\vec{q},\lambda)$ are given by

$$z = \pm\Big\{\big[\omega^2(\vec{q},\lambda)+\Sigma'(\vec{q},\lambda)\big]^2+\Sigma''^2(\vec{q},\lambda)\Big\}^{1/4}e^{\pm i\Psi(\vec{q},\lambda)} \tag{27}$$

where

$$\Psi(\vec{q},\lambda) = \frac{1}{2}tan^{-1}\left\{\frac{\Sigma''(\vec{q},\lambda)}{\omega^2(\vec{q},\lambda)+\Sigma'(\vec{q},\lambda)}\right\}. \tag{28}$$

Here $\Sigma'(\vec{q},\lambda)$ and $\Sigma''(\vec{q},\lambda)$ stand for $\Sigma'(\vec{q},\lambda;\omega)$ and $\Sigma''(\vec{q},\lambda;\omega)$ with $\omega=\omega(\vec{q},\lambda)$.

For the in-plane modes $\lambda=\{\mathrm{L},\mathrm{T}\}$, where the harmonic phonon dispersion is linear in the long wavelength regime, we obtain the renormalized phonon frequency

$$\Omega(\vec{q},\lambda) = \omega(\vec{q},\lambda)+\Delta(\vec{q},\lambda) \tag{29}$$

where

$$\Delta(\vec{q},\lambda) = \frac{\Sigma'(\vec{q},\lambda)}{2\omega(\vec{q},\lambda)}, \tag{30}$$

is the phonon frequency shift.

The phonon damping (line-width) is given by

$$\Gamma(\vec{q},\lambda) = -\frac{\Sigma''(\vec{q},\lambda)}{2\omega(\vec{q},\lambda)}. \tag{31}$$

Expressions corresponding to Eqs. (29)-(31) for $\Delta(\vec{q},\lambda)$ and $\Gamma(\vec{q},\lambda)$ have been obtained originally by diagrammatic techniques for 3D anharmonic crystals[40,41].

For the out-of-plane mode (λ=Z), $\Sigma'(\vec{q},\mathrm{Z})$ is quadratic in q (see Sect. VI) and cannot be treated as a perturbation to $\omega^2(\vec{q},\mathrm{Z})$=$\kappa_0 q^4$ in the long wavelength regime. We write

$$\Sigma'(\vec{q},\mathrm{Z}) \equiv q^2 c_{\mathrm{Z}}^2 \tag{32}$$

where c_{Z}, to be determined later, has the dimension of a velocity. In case that $\Sigma''(\vec{q},\mathrm{Z})$ in Eq. (27) can be neglected, we define the renormalized flexural mode frequency

$$\Omega(\vec{q},\mathrm{Z}) = \sqrt{\omega^2(\vec{q},\mathrm{Z})+q^2c_{\mathrm{Z}}^2}. \tag{33}$$

For short wavelengths $q >> q_c$ where

$$q_c = c_{\mathrm{Z}}\sqrt{\frac{2}{\kappa_0}}, \tag{34}$$

$\Omega(\vec{q},\mathrm{Z})$ reduces to $\omega(\vec{q},\mathrm{Z}) = \sqrt{\kappa_0}q^2$. At long wavelengths $q << q_c$ the dispersion becomes linear

$$\Omega(\vec{q},\mathrm{Z}) = c_{\mathrm{Z}}q. \tag{35}$$

In the intermediate regime where $q_c/2 < q < q_c$ we obtain from Eq. (27) $\Omega(\vec{q},\mathrm{Z}) = \sqrt{\kappa_o q_c}q^{3/2}$. These results are familiar from first order perturbation theory in crystalline membranes[22]. Concepts from membrane theory have been applied to the continuum theory of graphene[17,20,42] and graphene nanoribbons[43].

In Sect. VI B., we will show that c_{Z} depends on temperature and on the size of the system.

B_α	B_1	B_2	B_3
$\varphi^{(3)}_{xxx}(A;B_\alpha)$	$f^{(3)}=124.12$	$\frac{-1}{8}(f^{(3)}+9g^{(3)})$	$\frac{-1}{8}(f^{(3)}+9g^{(3)})$
$\varphi^{(3)}_{xyy}(A;B_\alpha)$	$g^{(3)}=40.43$	$\frac{-1}{8}(3f^{(3)}-5g^{(3)})$	$\frac{-1}{8}(3f^{(3)}-5g^{(3)})$
$\varphi^{(3)}_{xxy}(A;B_\alpha)$	/	$\frac{\sqrt{3}}{8}(f^{(3)}+g^{(3)})$	$\frac{-\sqrt{3}}{8}(f^{(3)}+g^{(3)})$
$\varphi^{(3)}_{yyy}(A;B_\alpha)$	/	$\frac{3\sqrt{3}}{8}(f^{(3)}+g^{(3)})$	$\frac{-3\sqrt{3}}{8}(f^{(3)}+g^{(3)})$
$\varphi^{(3)}_{zzx}(A;B_\alpha)$	$h^{(3)}=-3.35$	$\frac{-1}{2}h^{(3)}$	$\frac{-1}{2}h^{(3)}$
$\varphi^{(3)}_{zzy}(A;B_\alpha)$	/	$\frac{\sqrt{3}}{2}h^{(3)}$	$\frac{-\sqrt{3}}{2}h^{(3)}$

TABLE I: Third order anharmonic force constants for nearest neighbor atoms. Numerical values are for graphene and are in units of 10^{12} erg/cm^3.

IV. INTERACTION PARAMETERS

We will use phonon dispersions[35] calculated by means of an harmonic force constant model (Fig. 1). Such a force constant model has been suggested from in-plane inelastic X-ray scattering experiments in graphite[25].

In the absence of an empirical model for the anharmonic coupling parameters $\Phi^{(3)}_{ijk}(\vec{n_1}\kappa_1;\vec{n_2}\kappa_2;\vec{n_3}\kappa_3)$ and $\Phi^{(4)}_{ijkl}(\vec{n_1}\kappa_1;\vec{n_2}\kappa_2;\vec{n_3}\kappa_3;\vec{n_4}\kappa_4)$, we take an heuristic approach. We assume a central force inter-atomic potential, where the potential function of interaction $\varphi(\vec{n_1}\kappa_1;\vec{n_2}\kappa_2)$ between an atom κ' at site $\vec{X}(\vec{n'}\kappa')$ and an atom κ at site $\vec{X}(\vec{n}\kappa)$ depends only on the interatomic distance $r=|\vec{X}(\vec{n}\kappa)-\vec{X}'(\vec{n}'\kappa')|$. One has[2]

$$\Phi^{(3)}_{ijk}(\vec{n}\kappa;\vec{n}\kappa;\vec{n'}\kappa') = -\varphi^{(3)}_{ijk}(\vec{n}\kappa;\vec{n'}\kappa') \quad (\vec{n}\kappa)\neq(\vec{n'}\kappa') \tag{36a}$$

$$\Phi^{(3)}_{ijk}(\vec{n}\kappa;\vec{n}\kappa;\vec{n}\kappa) = {\sum_{\vec{n'}\kappa'}}' \varphi^{(3)}_{ijk}(\vec{n}\kappa;\vec{n'}\kappa') \tag{36b}$$

Here $\varphi^{(3)}_{ijk}$ are the third order derivatives of the potential $\varphi(r)$. Similarly one has

$$\Phi^{(4)}_{ijkl}(\vec{n}\kappa;\vec{n}\kappa;\vec{n}\kappa;\vec{n'}\kappa') = -\varphi^{(4)}_{ijkl}(\vec{n}\kappa;\vec{n'}\kappa') \quad (\vec{n}\kappa)\neq(\vec{n'}\kappa') \tag{37a}$$

$$\Phi^{(4)}_{ijkl}(\vec{n}\kappa;\vec{n}\kappa;\vec{n'}\kappa';\vec{n'}\kappa') = \varphi^{(4)}_{ijkl}(\vec{n}\kappa;\vec{n'}\kappa') \quad (\vec{n}\kappa)\neq(\vec{n'}\kappa') \tag{37b}$$

$$\Phi^{(4)}_{ijkl}(\vec{n}\kappa;\vec{n}\kappa;\vec{n}\kappa;\vec{n}\kappa) = {\sum_{\vec{n'}\kappa'}}' \varphi^{(4)}_{ijkl}(\vec{n}\kappa;\vec{n'}\kappa'). \tag{37c}$$

All these quantities are invariant with respect to a permutation of the indices $i,j,\ldots$.

Using Eqs. (36a), (36b) and (11) we get

$$\Phi^{(3)}_{ijk}\begin{pmatrix}AAA\\ \vec{q}_1\vec{q}_2\vec{q}_3\end{pmatrix} = \frac{1}{\sqrt{M_C^3}}\sum_\alpha \varphi^{(3)}_{ijk}(A;B_\alpha)\Delta(\vec{q}_1+\vec{q}_2+\vec{q}_3), \tag{38a}$$

$$\Phi^{(3)}_{ijk}\begin{pmatrix}BAA\\ \vec{q}_1\vec{q}_2\vec{q}_3\end{pmatrix} = \frac{-1}{\sqrt{M_C^3}}\sum_\alpha \varphi^{(3)}_{ijk}(A;B_\alpha)e^{i\vec{q_1}\cdot\vec{r}(B_\alpha)}\Delta(\vec{q}_1+\vec{q}_2+\vec{q}_3), \tag{38b}$$

etc. for $\Phi^{(3)}_{ijk}\left(\begin{smallmatrix}BBA\\ \vec{q}_1\vec{q}_2\vec{q}_3\end{smallmatrix}\right)$, $\Phi^{(3)}_{ijk}\left(\begin{smallmatrix}BBB\\ \vec{q}_1\vec{q}_2\vec{q}_3\end{smallmatrix}\right)$.

Similarly we obtain from Eqs. (15) and (37a)-(37c)

B_α	B_1	B_2
$\varphi^{(4)}_{xxxx}(A;B_\alpha)$	$j^{(4)} = f_r/r_a^2 = 20.56$	$\frac{1}{16}(j^{(4)} + 9k^{(4)} + 18m^{(4)})$
$\varphi^{(4)}_{yyyy}(A;B_\alpha)$	$k^{(4)} = f_i/r_a^2 = 6.69$	$\frac{1}{16}(9j^{(4)} + k^{(4)} + 18m^{(4)})$
$\varphi^{(4)}_{xxyy}(A;B_\alpha)$	$m^{(4)} = \sqrt{f_i f_r}/r_a^2 = 7.32$	$\frac{1}{16}(3j^{(4)} + 3k^{(4)} - 2m^{(4)})$
$\varphi^{(4)}_{xxzz}(A;B_\alpha)$	$n^{(4)} = \sqrt{f_r f_o}/r_a^2 = 6.27$	$\frac{1}{4}(n^{(4)} + 3p^{(4)})$
$\varphi^{(4)}_{yyzz}(A;B_\alpha)$	$p^{(4)} = \sqrt{f_i f_o}/r_a^2 = 3.58$	$\frac{1}{4}(p^{(4)} + 3n^{(4)})$
$\varphi^{(4)}_{zzzz}(A;B_\alpha)$	$l^{(4)} = f_o/r_a^2 = 3.06$	$l^{(4)}$

TABLE II: Fourth order anharmonic force constants for nearest neighbor atoms. Due to symmetry $\varphi^{(4)}_{\cdots}(A;B_3) = \varphi^{(4)}_{\cdots}(A;B_2)$. Numerical values are for graphene and are in units of 10^{20} erg/cm^4.

$$\Phi^{(4)}_{ijkl}\begin{pmatrix} AAAA \\ \vec{q}_1\vec{q}_2\vec{q}_3\vec{q}_4 \end{pmatrix} = \frac{1}{M_C^2}\sum_\alpha \varphi^{(4)}_{ijk}(A;B_\alpha)\Delta(\vec{q}_1+\vec{q}_2+\vec{q}_3+\vec{q}_4), \tag{39a}$$

$$\Phi^{(4)}_{ijkl}\begin{pmatrix} BAAA \\ \vec{q}_1\vec{q}_2\vec{q}_3\vec{q}_4 \end{pmatrix} = \frac{-1}{M_C^2}\sum_\alpha \varphi^{(4)}_{ijk}(A;B_\alpha)e^{i\vec{q_1}\cdot\vec{r}(B_\alpha)}\Delta(\vec{q}_1+\vec{q}_2+\vec{q}_3+\vec{q}_4). \tag{39b}$$

Replacement of $\Phi^{(n)}\binom{\cdots A\cdots}{\cdots\vec{q}\cdots}$ by $\Phi^{(n)}\binom{\cdots B\cdots}{\cdots\vec{q}\cdots}$ leads to an additional phase factor $e^{i\vec{q}\cdot\vec{r}(\mathrm{B}_\alpha)}$ on the right hand side.

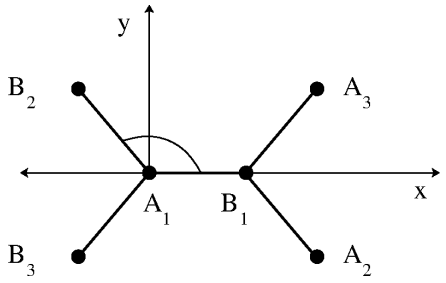

FIG. 2: Schematic plot of A_1 and B_1 atoms belonging to the unit cell with its corresponding first-nearest neighbors.

For interactions between nearest neighbor atoms A and B_1, at equilibrium positions $(0,0)$ and $a/\sqrt{3},0$ respectively (Fig. 2) we retain $\varphi^{(3)}_{xxx}(A;B_1) = f^{(3)}$; $\varphi^{(3)}_{xyy}(A;B_1) = g^{(3)}$; $\varphi^{(3)}_{xzz}(A;B_1) = h^{(3)}$. The interactions between A and B_2 at $(-a/2\sqrt{3}, a/2)$ as well as between A and B_3 at $(-a/2\sqrt{3}, -a/2)$ are obtained by using the transformation laws of third rank tensors under rotations by $\pm 120°$, respectively. The results are summarized in Table I. The numerical values of $f^{(3)}$, $g^{(3)}$ and $h^{(3)}$ are for the 2D crystal graphene and are determined from the acoustic mode Grüneisen parameters (see Sect. V).

The negative value of $h^{(3)}$ is motivated by an argument originally put forward by I. M. Lifshitz (Ref. 13) in formulating the dispersion law for layered structures in the long wavelength limit. In the present case of a discrete crystal structure the force in the x-direction on atom B_1 due to an out-of-plane displacement of atom A_1 (Fig. 2) reads $M_C\ddot{u}_x(B_1) = -\Phi^{(3)}_{zzx}(A_1;A_1;B_1)u_z^2(A_1)$. Since this force has to be attractive, $-\Phi^{(3)}_{zzx}(A_1;A_1;B_1) = \varphi^{(3)}_{zzx} \equiv h^{(3)} < 0$. In Sect. V we will see that the negative value of $h^{(3)}$ is related to a negative value of the out-of-plane Grüneisen coefficient $\gamma(\vec{q},\mathrm{Z})$ and hence, as has been emphasized by Mounet and Marzari (Ref. 14), favors a negative contribution to the thermal expansion.

Numerical values of the fourth order force constants $j^{(4)}, k^{(4)}, ..., l^{(4)}$ are estimated as shown in Table II by dividing the second order force constant of graphene[25] by the square of the C-C bond distance. In analogy with the reasoning about $\varphi^{(3)}_{zzx}$ we consider the force $-\Phi^{(4)}_{zzxx}(A_1;A_1;B_1;B_1) \times u_z^2(A_1)u_x(B_1) < 0$ where $u_x(B_1) > 0$. By means of Eq. (37b) follows $\varphi^{(4)}_{zzxx}(A_1;A_1;B_1;B_1) = n^{(4)} > 0$. The same holds for $p^{(4)}$.

V. THERMAL EXPANSION

Here we present analytical calculations of the generalized Grüneisen coefficients and the thermal expansion. Although we explicitly discuss graphene, the analytical results are applicable to other layered 2D crystals with D_{3h} symmetry by replacing M_C by 2μ, where μ is the reduced mass, and by adapting the corresponding numerical values for the material constants.

We will need the anharmonic coupling coefficients for acoustic phonons in the long wavelength regime. We use $e_i^A(\vec{k},\lambda) = e_i^B(\vec{k},\lambda)$ as well as $e_i^A(\vec{k}-\vec{q},\lambda) \sim e_i^A(\vec{k},\lambda)$ for $\vec{q}\to 0$. From Eqs. (10), (11) and (36a), (36b) we obtain

$$\Phi^{(3)}\begin{pmatrix}\lambda & \lambda_1 & \lambda_2\\ -\vec{q} & \vec{k} & \vec{q}-\vec{k}\end{pmatrix} = \frac{i\sqrt{2}}{4\sqrt{M_C^3\omega(\vec{q},\lambda)\omega(\vec{k},\lambda_1)\omega(\vec{q}-\vec{k},\lambda_2)}} \times \sum_\alpha \sum_{ijk} e_i^{A*}(\vec{q},\lambda) e_j^A(\vec{k},\lambda_1) e_k^{A*}(\vec{k},\lambda_2)\ \varphi_{ijk}^{(3)}(A;B_\alpha)(\vec{q}\cdot\vec{r}(B_\alpha))(\vec{k}\cdot\vec{r}(B_\alpha))((\vec{k}-\vec{q})\cdot\vec{r}(B_\alpha)). \quad (40)$$

We have performed a series expansion in $\vec{q}$ and in $\vec{k}$ of the exponentials. Similarly we proceed with Eqs. (14), (15) and (37a)-(37c) and obtain

$$\Phi^{(4)}\begin{pmatrix}\lambda & \lambda' & \lambda' & \lambda\\ -\vec{q} & \vec{k} & -\vec{k} & \vec{q}\end{pmatrix} = \frac{1}{4M_C^2\omega(\vec{q},\lambda)\omega(\vec{k},\lambda')} \times \sum_\alpha \sum_{ijkl} e_i^{A*}(\vec{q},\lambda) e_j^A(\vec{k},\lambda') e_k^{A*}(\vec{k},\lambda') e_l^A(\vec{q},\lambda)\ \varphi_{ijkl}^{(4)}(A;B_\alpha)(\vec{q}\cdot\vec{r}(B_\alpha))^2(\vec{k}\cdot\vec{r}(B_\alpha))^2. \quad (41)$$

In Sect. III we have seen that the thermal tension β_T and equivalently the thermal expansion α_T depend linearly on the third order anharmonicities through the generalized Grüneisen coefficient $\gamma(\vec{q},\lambda)$, Eq. (20). From Eq.(A-9) we obtain in the long wavelength regime

$$\frac{\partial\omega(\vec{q},\lambda)}{\partial\epsilon_{ii}} = -\frac{1}{4\omega(\vec{q},\lambda)M_C}\sum_\alpha\sum_{kl}\varphi_{kli}^{(3)}(A;B_\alpha) r_i(B_\alpha) e_k^{A*}(\vec{q},\lambda) e_l^A(\vec{q},\lambda)(\vec{q}\cdot\vec{r}(B_\alpha))^2. \quad (42)$$

Here $\vec{r}(B_\alpha)$, $\alpha = 1,2,3$ runs over the three nearest neighbor atoms B_α of A_1 (see Fig. (2)).

In order to obtain quantitative results for β_T one has to evaluate the $\vec{q}$-sum in Eq. (18). We have used analytical methods which allow us to investigate the limit cases of high and low T and to discuss singularities in $\vec{q}$-space.

We start from Eq. (42) with the out-of-plane mode λ=Z. The polarization vectors in the long wavelength regime are $e_k^\kappa(\vec{0},\mathrm{Z}) = \sqrt{1/2}\delta_{kz}$ for κ =A, B. Carrying out the summation over neighbor atoms using Table I, we obtain

$$\frac{\partial\omega(\vec{q},\mathrm{Z})}{\partial\epsilon_{xx}} = \frac{-a^3h^{(3)}}{64\sqrt{3}M_C\omega(\vec{q},\mathrm{Z})}\left[3q_x^2+q_y^2\right]. \quad (43)$$

Since $h^{(3)}$, the anharmonic force constant φ_{zzx} is negative, the frequency $\omega(\vec{q},\mathrm{Z})$ increases with in-plane strain. The corresponding expression for $\partial\omega(\vec{q},\mathrm{Z})/\partial\epsilon_{yy}$ is obtained by an interchange of $q_x^2 \leftrightarrow q_y^2$ in Eq. (43). Addition of both contributions and use of Eq. (20) leads to

$$\gamma(\vec{q},\mathrm{Z}) = \frac{a^3h^{(3)}q^2}{16\sqrt{3}M_C\omega^2(\vec{q},\mathrm{Z})}, \quad (44)$$

where $q^2 = q_x^2+q_y^2$. Since $\omega^2(\vec{q},\mathrm{Z}) = \kappa_0 q^4$, the wave vector average of $\gamma(\vec{q},\mathrm{Z})$ diverges logarithmically with $q\to 0$. We then consider a finite 2D crystal with linear dimensions l. The corresponding wave vector $q_l = 2\pi/l$ entails a lowest non-zero frequency $\omega_l(\mathrm{Z}) = \sqrt{\kappa_0}q_l^2$. Transforming the $\vec{q}$-sum in a frequency integral, the wave vector average of Eq. (44) reads

$$\overline{\gamma(\mathrm{Z})} = \frac{\tilde{\gamma}(\mathrm{Z})v_{2D}}{4\pi\kappa_0} ln\left(\frac{\omega_s(\mathrm{Z})}{\omega_l(\mathrm{Z})}\right), \quad (45)$$

where $\tilde{\gamma}(\mathrm{Z}) = a^3h^{(3)}/(16\sqrt{3}M_C)$. We take for $\overline{\gamma(\mathrm{Z})}$ the empirical numerical value γ_{ZA}=-1.5 from Ref. 26. As

upper frequency limit we choose ω_s(Z)=94.3 THz, which corresponds to $\tilde{\nu}$=500 cm^{-1} for the ZA branch in Fig. 1. With $l = 10^4 a$ the lower frequency limit is ω_l(Z)=4.25 MHz. Solving Eq. (45) with respect to $h^{(3)}$, we obtain the value quoted in Table I.

Considering the in-plane displacement modes T and L we use in the long wavelength regime the polarization vectors $e_k^\kappa(\vec{0},\mathrm{T}) = \sqrt{1/2}\delta_{ky}$ and $e_k^\kappa(\vec{0},\mathrm{L}) = \sqrt{1/2}\delta_{kx}$, for κ =A, B. Proceeding as before we obtain

$$\gamma(\vec{q},\mathrm{T}) = \frac{a^3}{64\sqrt{3}M_C\omega^2(\vec{q},\mathrm{T})} \times\left[(f^{(3)}+3g^{(3)})q_x^2+(3f^{(3)}+g^{(3)})q_y^2\right]. \quad (46)$$

The expression for $\gamma(\vec{q},\mathrm{L})$ is obtained from Eq. (46) by interchange of $q_x^2 \leftrightarrow q_y^2$ and by replacing $\omega(\vec{q},\mathrm{T})$ by $\omega(\vec{q},\mathrm{L})$. The long wavelength acoustic phonons in a 2D crystal have frequencies $\omega(\vec{q},\mathrm{T}) = c_\mathrm{T} q$ and $\omega(\vec{q},\mathrm{L}) = c_\mathrm{L} q$, where c_T and c_L are the transversal and longitudinal sound velocities. Using the Debye interpolation scheme we define an average sound velocity $\hat{c}$ by

$$\frac{2}{\hat{c}^2} = \frac{1}{c_\mathrm{L}^2} + \frac{1}{c_\mathrm{T}^2}, \quad (47)$$

and replace both $\omega(\vec{q},\mathrm{T})$ and $\omega(\vec{q},\mathrm{L})$ by $\hat{c}q$. With the model of Ref. 35 we have $c_\mathrm{L} = 23.1\times10^5$ cm s^{-1}, $c_\mathrm{T} = 14.3\times10^5$ cm s^{-1} and hence $\hat{c} = 17.2\times10^5$ cm s^{-1}.

Adding the long wavelength expressions for $\gamma(\vec{q},\mathrm{T})$ and $\gamma(\vec{q},\mathrm{L})$ we obtain the in-plane Grüneisen constant $\gamma(\perp)$ which is independent of the wave vector:

$$\gamma(\perp) = \frac{a^3(f^{(3)}+g^{(3)})}{16\sqrt{3}M_C\hat{c}^2}. \quad (48)$$

Here and in the following $\perp$ has the meaning of in-plane, i. e. normal to the highest symmetry axis. We identify $\gamma(\perp)$, Eq. (48) with the average $(\gamma_\mathrm{LA}+\gamma_\mathrm{TA})/2$=1.5, taken from Ref. 26. Comparison with Eq. (48) yields $(f^{(3)}+g^{(3)})$=164.55×10^{12} erg/cm^3. Assuming that the ratio $f^{(3)}/g^{(3)}$ is equal to 25.88/8.42=3.07 as inferred from the second order stretching and shearing force constants[25], we obtain the values quoted in Table I.

Conversely we have used the present values of $f^{(3)}$ and $g^{(3)}$ to calculate the E_{2g} in-plane optical mode Grüneisen parameter (biaxial stress) and obtain $\gamma(E_{2g})$=1.51. We recall that the in-plane E_{2g} Grüneisen parameter inferred from Raman scattering spectra on graphite under hydrostatic pressure[44] leads to $\gamma(E_{2g})$=1.59, as quoted in Ref. 33. Raman spectroscopy on uniaxially strained graphene[45] leads to $\gamma(E_{2g})$=1.99.

We turn now to the thermal tension defined by Eq. (18). Given the different analytic behavior of $\gamma(\vec{q},\mathrm{Z})$ and $\gamma(\perp)$ we will consider separately the out-of-plane contributions to β_T by writing

$$\beta_T = \beta_T(\mathrm{Z}) + \beta_T(\perp) \quad (49)$$

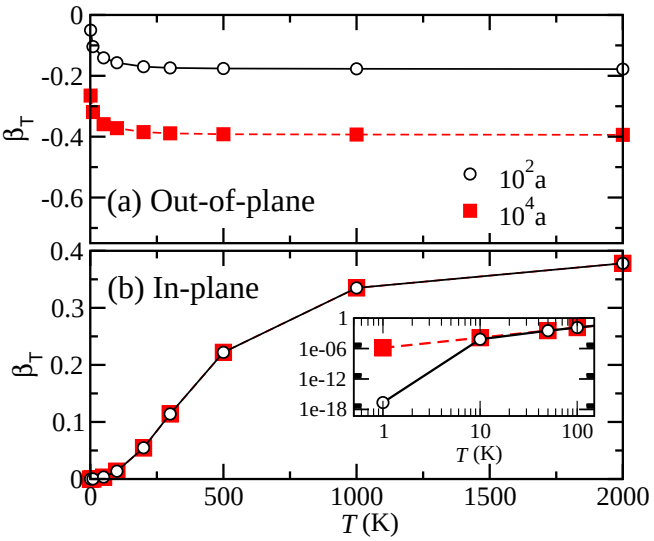

FIG. 3: (Color online) Thermal tension coefficient β_T for system sizes l=10$^2 a$ (circles) and 10$^4 a$ (squares). The (a) out-of-plane β_T(Z) and (b) in-plane $\beta_T(\perp)$ components are given in units of dyn cm^{-1} K^{-1}. Notice in the inset the size dependence at low T of $\beta_T(\perp)$.

with $\beta_T(\perp) = \beta_T(\mathrm{T})+\beta_T(\mathrm{L})$. We start with λ=Z. Transforming the $\vec{q}$-sum into a frequency integral we get

$$\beta_T(\mathrm{Z}) = \frac{\tilde{\gamma}(\mathrm{Z})\hbar^2}{4\pi k_B T^2\kappa_0}\int_{\omega_l(\mathrm{Z})}^{\omega_s(\mathrm{Z})} d\omega \frac{\omega e^{\hbar\omega/k_BT}}{(e^{\hbar\omega/k_BT}-1)^2}. \quad (50)$$

Here and in the following we use the third order anharmonic force constants from Table I. Then $\tilde{\gamma}$(Z)=-9.03×10^{10}cm^{2}s^{-2} which implies that β_T(Z) is negative. The size dependence is accounted for by ω_l(Z). In the high T limit (classical case), $k_BT > \hbar\omega$, this expression reduces to

$$\beta_T(\mathrm{Z}) = \frac{\tilde{\gamma}(\mathrm{Z})}{\kappa_0}\frac{k_B}{4\pi} ln\left(\frac{\omega_s(\mathrm{Z})}{\omega_l(\mathrm{Z})}\right), \quad (51)$$

and in the low T limit (quantum case), $k_BT < \hbar\omega_l(\mathrm{Z}) < \hbar\omega_s(\mathrm{Z})$,

$$\beta_T(\mathrm{Z}) = \frac{\tilde{\gamma}(\mathrm{Z})}{\kappa_0}\frac{\hbar\omega_l(\mathrm{Z})}{4\pi T} e^{-\hbar\omega_l(\mathrm{Z})/k_BT}. \quad (52)$$

While β_T(Z) is constant at high T, it vanishes with $T \to 0$, in accordance with Nernst's theorem[46]. In Fig. 3(a) we plotted β_T(Z), Eq. (50), as function of temperature for two different crystal sizes.

In studying the contribution $\beta_T(\perp)$ due to the in-plane modes we make use of the linear dispersion and replace $\omega(\vec{q},\mathrm{T})$ and $\omega(\vec{q},\mathrm{L})$ by $\hat{c}q$. The upper frequency limit is $\omega_s(\perp) = (4\pi\hat{c}^2/v_{2D})^{1/2}$. For the sake of consistency we take a crystal with finite size where $\omega_l(\perp) = \hat{c}\ 2\pi/l$. We then obtain

$$\beta_T(\perp) = \frac{\gamma(\perp)\hbar^2}{2\pi\hat{c}^2 k_B T^2}\int_{\omega_l(\perp)}^{\omega_s(\perp)} d\omega \frac{\omega^3 e^{\hbar\omega/k_BT}}{\left(e^{\hbar\omega/k_BT}-1\right)^2}, \quad (53)$$

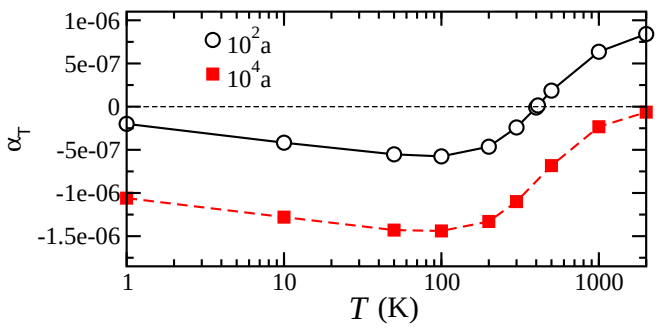

FIG. 4: (Color online) Thermal expansion coefficient α_T for l=10^2a and 10^4a sample sizes. Units K^{-1}.

where $\gamma(\perp)$=1.5, which implies that $\beta_T(\perp)$ is positive. In contradistinction with Eq. (50) the integral exists also for $\omega_l(\perp) = 0$, i. e. for $l \to \infty$. In the high T regime where $k_BT > \hbar\omega_s(\perp) > \hbar\omega_l(\perp)$ we obtain

$$\beta_T(\perp) = \frac{\gamma(\perp)k_B}{v_{2D}}\left(1 - \pi\frac{v_{2D}}{l^2}\right) \tag{54}$$

In the low T regime $k_BT < \hbar\omega_l(\perp) < \hbar\omega_s(\perp)$ we obtain

$$\beta_T(\perp) = \frac{\gamma(\perp)\hbar}{2\pi\hat{c}^2T}\omega_l^3(\perp)e^{-\hbar\omega_l(\perp)/k_BT}. \tag{55}$$

In Fig. 3 (b) we plotted $\beta_T(\perp)$, Eq. (53), as function of T for two different crystal sizes. Notice here again the agreement with the limit cases Eqs. (54) and (55) of high and low T, respectively. In particular it follows from Eq. (54) that $\beta_T(\perp)$ is quasi size independent at large T.

Evaluation of Eqs.(50) and (53) shows that $|\beta_T(\mathrm{Z})| > \beta_T(\perp)$ at low T and hence β_T, Eq. (49) is negative. A change of sign to positive values becomes possible with increasing temperature. Solution of the equation

$$|\beta_T(\mathrm{Z};T,l)| = \beta_T(\perp;T,l) \tag{56}$$

yields pairs of values $\{T_\alpha, l_\alpha\}$ where β_T, Eq. (49), changes sign, (Fig. 4). Here T_α is an implicit function of l_α. We obtain $\{l_\alpha = 10^2a, T_\alpha = 407\mathrm{K}\}$; $\{l_\alpha = 10^3a, T_\alpha = 697\mathrm{K}\}$. In case of an infinite system (thermodynamic limit), $\beta_T(\mathrm{Z})$ diverges logarithmically (see Eq. (51)). Then Eq. (56) has no solution and β_T remains negative up to highest T. With our model parameters we find that for $l = 10^4a$, T_α becomes already unphysically large (10^4 K).

We will show below (Sect. VI) that the renormalization of the flexural mode however decreases $|\beta_T(\mathrm{Z})|$ and results in room temperature values of T_α for graphene samples of macroscopic size. Since the ratio $|\beta_T(\mathrm{Z})|$ versus $\beta_T(\perp)$ depends on material constants, it is conceivable that for some finite size monolayer materials $|\beta_T(\mathrm{Z})| < \beta_T(\perp)$ always holds and the thermal expansion is positive, as has been concluded[47] for MoS_2.

VI. FREQUENCY SHIFTS AND LINEWIDTHS

Phonon lineshifts are due to third and fourth order anharmonicities and phonon dampings due to third order.

A. In-plane modes

We study the case where a long wavelength in-plane phonon (λ =L, T) of wavevector $\vec{q}$ decays into two out-of-plane phonons (λ =Z) with wave vectors $\vec{k}$ and $\vec{q}-\vec{k}$. Since all wave vectors are small, there are no Umklapp processes. The frequency shift due to third order anharmonicities, obtained by means of Eqs. (30), (23) and (24), reads

$$\Delta^{(3)}(\vec{q},\lambda) = \frac{\hbar}{2N}P\sum_{\vec{k}}\left|\Phi^{(3)}\begin{pmatrix}\lambda & \mathrm{Z} & \mathrm{Z}\\ -\vec{q} & \vec{k} & \vec{q}-\vec{k}\end{pmatrix}\right|^2 \times\left\{\frac{1+n(\vec{k},\mathrm{Z})+n(\vec{k}-\vec{q},\mathrm{Z})}{\omega(\vec{q},\lambda)-\omega(\vec{k},\mathrm{Z})-\omega(\vec{k}-\vec{q},\mathrm{Z})}\right\}. \tag{57}$$

With $\vec{q} = (q, 0)$ taken as polar axis along the x-direction, we have $\vec{k} = k(cos\ \varphi, sin\ \varphi)$. We approximate the polarization vectors entering $\left|\Phi^{(3)}\left(\begin{smallmatrix}\lambda & \mathrm{Z} & \mathrm{Z}\\ -\vec{q} & \vec{k} & \vec{q}-\vec{k}\end{smallmatrix}\right)\right|$ by $e_i^A(\vec{q},\lambda) = \sqrt{1/2}\delta_{i\zeta}$, with $\zeta = x$ for λ =L and $\zeta = y$ for λ =T. Furthermore, we use $e_j^A(\vec{k},\mathrm{Z}) \approx e_j^A(\vec{k}-\vec{q},\mathrm{Z}) \approx \sqrt{1/2}\delta_{jz}$, approximate $\omega(\vec{k}-\vec{q},\mathrm{Z})$ by $\omega(\vec{k},\mathrm{Z})$ and $sin^2(\vec{k}\cdot\vec{r}(B_\alpha))$ by $(\vec{k}\cdot\vec{r}(B_\alpha))^2$. From Eq. (40) we then obtain for λ =L

$$\Phi^{(3)}\begin{pmatrix}\mathrm{L} & \mathrm{Z} & \mathrm{Z}\\ -\vec{q} & \vec{k} & \vec{q}-\vec{k}\end{pmatrix} = \frac{i\sqrt{q}h^{(3)}a^3(2cos^2\varphi+1)}{64\sqrt{3M_C^3c_\mathrm{L}\kappa_0}} \tag{58}$$

The expression for λ = T is obtained from Eq. (58) replacing $(2cos^2\varphi+1)$ by 2 $cos\varphi\ sin\varphi$ and c_L by c_T. Transforming the $\vec{k}$-sum in Eq. (57) to a 2D integral, we have

$$\Delta^{(3)}(\vec{q},\lambda) = \frac{\hbar qC^{(3)}(\lambda)}{2}P\int_{\omega_l(\mathrm{Z})}^{\omega_s(\mathrm{Z})}d\omega\frac{(1+2n(\omega))}{\omega(\vec{q},\lambda)-2\omega} \tag{59}$$

where $n(\omega) = (e^{\hbar\omega/k_BT}-1)^{-1}$. Here we have defined for λ=L

$$C^{(3)}(\mathrm{L}) = \frac{(h^{(3)}a^4)^2 3\sqrt{3}}{\pi(256)^2c_\mathrm{L}M_C^3\kappa_o^{3/2}}, \tag{60}$$

while for λ=T, c_L has to be replaced by c_T and $3\sqrt{3}$ by $1/\sqrt{3}$. We obtain $C^3(\mathrm{L})$=7.51 × $10^{27}\mathrm{cm}^{-1}\mathrm{g}^{-1}$ and $C^3(\mathrm{T})$=1.35 × $10^{27}\mathrm{cm}^{-1}\mathrm{g}^{-1}$. Carrying out the integration we obtain in the quantum case

$$\Delta^{(3)}(\vec{q},\lambda) = \frac{\hbar q}{4}C^{(3)}(\lambda)ln\left(\frac{\omega(\vec{q},\lambda)-2\omega_l(\mathrm{Z})}{2\omega_s(\mathrm{Z})-\omega(\vec{q},\lambda)}.\right) \tag{61}$$

In the classical case we get

$$\Delta^{(3)}(\vec{q},\lambda) = \frac{k_BTC^{(3)}(\lambda)}{c_\lambda}ln\left(\frac{\omega_s(\mathrm{Z})[\omega(\vec{q},\lambda)-2\omega_l(\mathrm{Z})]}{\omega_l(\mathrm{Z})[2\omega_s(\mathrm{Z})-\omega(\vec{q},\lambda)]}\right). \tag{62}$$

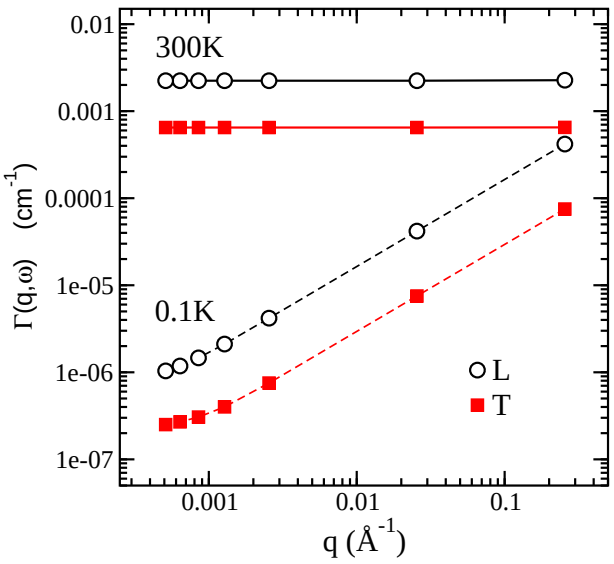

FIG. 5: (Color online) Linewidths for λ =L (circles) and T (squares) at different temperatures as indicated. The 2D crystal size is $l = 10^4 a$.

For T=1000 K and q=$\pi/10a$ we get $\Delta^{(3)}(\vec{q},\mathrm{L}) = 6.83 \times 10^9 \mathrm{s}^{-1}$ i. e.$3.6 \times 10^{-2}\mathrm{cm}^{-1}$, and $\Delta^{(3)}(\vec{q},\mathrm{T}) = 1.91 \times 10^9 \mathrm{s}^{-1}$ i. e.$1.00 \times 10^{-2}\mathrm{cm}^{-1}$.

Turning to the corresponding linewidth process we find by means of Eqs. (26) and (31)

$$\Gamma(\vec{q},\lambda) = \frac{\pi\hbar}{2N}\sum_{\vec{k}} \left|\Phi^{(3)}\begin{pmatrix} \lambda & \mathrm{Z} & \mathrm{Z} \\ -\vec{q} & \vec{k} & \vec{q}-\vec{k}\end{pmatrix}\right|^2 \times \Big(1 + n(\vec{k},\mathrm{Z}) + n(\vec{k}-\vec{q},\mathrm{Z})\Big) \times \delta\Big(\omega(\vec{q},\lambda) - \omega(\vec{k},\mathrm{Z}) - \omega(\vec{k}-\vec{q},\mathrm{Z})\Big). \quad (63a)$$

With the same approximations as outlined before we obtain [resume]

$$\Gamma(\vec{q},\lambda) = \frac{\pi}{4}\hbar q C^{(3)}(\lambda)\left[1 + 2n\left(\frac{\omega(\vec{q},\lambda)}{2}\right)\right] \quad (64a)$$

which in the quantum regime becomes

$$\Gamma(\vec{q},\lambda) = \frac{\pi}{4}\hbar q C^{(3)}(\lambda). \quad (65)$$

In the classical regime we get

$$\Gamma(\vec{q},\lambda) = \frac{\pi}{c_\lambda} k_B T C^{(3)}(\lambda), \quad (66)$$

the result is independent of the wave vector[18]. Plots of the linewidths evaluated by means of Eq. (64a) for λ =L and T are given in Fig. 5.

The frequency shift due to scattering of an in-plane phonon with a flexural mode (fourth order anharmonic process) reads

$$\Delta^{(4)}(\vec{q},\lambda) = \frac{\hbar}{2N}\sum_{\vec{k}} \Phi^{(4)}\begin{pmatrix} \lambda & \mathrm{Z} & \mathrm{Z} & \lambda \\ -\vec{q} & \vec{k} & -\vec{k} & \vec{q}\end{pmatrix}\big[1 + 2n(\vec{k},\mathrm{Z})\big]. \quad (67)$$

Using long wavelength approximations as before, we obtain from Eq. (41)

$$\Phi^{(4)}\begin{pmatrix} \mathrm{L} & \mathrm{Z} & \mathrm{Z} & \mathrm{L} \\ -\vec{q} & \vec{k} & -\vec{k} & \vec{q}\end{pmatrix} = \frac{qa^4}{16\times 96 M_C^2\sqrt{\kappa_0}c_\mathrm{L}} \times\Big[(11n^{(4)} + p^{(4)})cos^2\varphi + (n^{(4)} + 3p^{(4)})sin^2\varphi\Big]. \quad (68)$$

The expression for λ =T is obtained by replacing c_L by c_T and interchanging $n^{(4)}$ with $p^{(4)}$. The summation over the Brillouin zone in Eq. (67) is readily transformed into a frequency integral

$$\Delta^{(4)}(\vec{q},\lambda) = \hbar q C^{(4)}(\lambda)\int_{\omega_l(\mathrm{Z})}^{\omega_s(\mathrm{Z})} d\omega\ \Big[1 + 2n(\omega)\Big], \quad (69)$$

where for λ =L

$$C^{(4)}(\mathrm{L}) = \frac{a^6\sqrt{3}(3n^{(4)} + p^{(4)})}{128\times 96\pi M_C^2 c_\mathrm{L}\kappa_o}. \quad (70)$$

Again $C^{(4)}(\mathrm{T})$ is obtained by the substitutions just mentioned. In the quantum limit, $k_B T \ll \hbar\omega_l(\mathrm{Z})$, we have

$$\Delta^{(4)}(\vec{q},\lambda) = \hbar q C^{(4)}(\lambda)\Big[\omega_s(\mathrm{Z}) - \omega_l(\mathrm{Z})\Big], \quad (71)$$

and in the classical limit, $k_B T \gg \hbar\omega_s(\mathrm{Z})$,

$$\Delta^{(4)}(\vec{q},\lambda) = 2q k_B T C^{(4)}(\lambda)\ ln\left(\frac{\omega_s(\mathrm{Z})}{\omega_l(\mathrm{Z})}\right). \quad (72)$$

Notice in both cases the linear dependence on the wave vector of the in-plane mode. Since $n^{(4)}$ and $p^{(4)}$ are positive (see Table II), we conclude that the lineshifts above are positive.

B. Flexural mode

We first investigate the decay and the lineshift of the flexural mode due to third order anharmonicities. As already emphasized[18], the scattering rate us dominated by the absorption processes ZA+ZA→LA(TA). The frequency dependent self-energy (See Sect. III, B) reads

$$\Sigma^{(3)}(\vec{q},\mathrm{Z};z) = \frac{2\hbar\omega(\vec{q},\mathrm{Z})}{N}\sum_{\vec{k}\lambda}\left|\Phi^{(3)}\begin{pmatrix} \mathrm{Z} & \mathrm{Z} & \lambda \\ \vec{q} & \vec{k}-\vec{q} & -\vec{k}\end{pmatrix}\right|^2 \times\frac{n(\vec{k}-\vec{q},\mathrm{Z}) - n(\vec{k},\mathrm{Z})}{z + \omega(\vec{k}-\vec{q},\mathrm{Z}) - \omega(\vec{k},\lambda)} \quad (73)$$

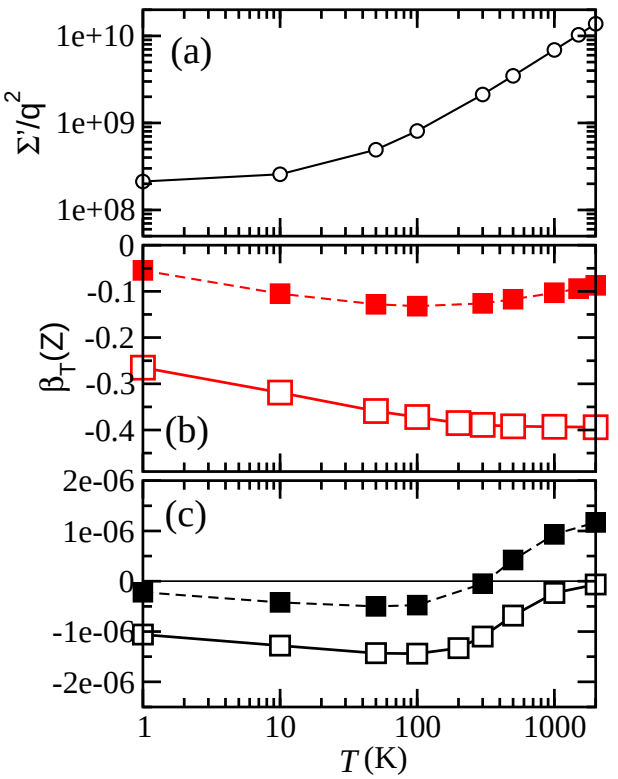

FIG. 6: (a) Quantity $c_{\rm Z}^2{=}\Sigma'(\vec{q},{\rm Z})/q^2$ as function of T, units cm^2 s^{-2}. (b) Thermal tension $\beta_T({\rm Z})$ and (c) thermal expansion α_T evaluated with renormalized flexural mode frequency $\Omega(\vec{q},{\rm Z})$ (filled squares) as function of T. $\beta_T({\rm Z})$ is given in units of dyn cm^{-1} K^{-1} and α_T in K^{-1}. The 2D crystal size is $l=10^4a$. Compare with Fig. 4.

where $z=\omega+i\epsilon$, $\epsilon\to 0^+$, and λ =L(T). We investigate this quantity for $\omega=\omega(\vec{q},{\rm Z})$. In order to get an analytically tractable problem, we take $\vec{q}=(q,0,0)$. In addition we replace $(\vec{k}-\vec{q})\cdot\vec{r}(B_\alpha)$ in Eq. (40) by its supremum $|\vec{k}-\vec{q}||\vec{r}(B_\alpha)|$. As consequence of these approximations only the scattering into the L mode is different from zero. From the study of $\Sigma^{(3)''}$ we obtain the decay rate (compare Eq. (31))

$$\Gamma(\vec{q},{\rm Z})=\hbar q^4\frac{128\kappa_0^{3/2}}{9c_{\rm L}^3}C^{(3)}({\rm L})csch\left(\frac{\hbar\omega(q,{\rm Z})}{k_BT}\right) \qquad (74)$$

In the classical regime we get

$$\Gamma(\vec{q},{\rm Z})=q^2k_BT\frac{128\pi\kappa_0}{9c_{\rm L}^3}C^{(3)}({\rm L}) \qquad (75)$$

and in the quantum regime

$$\Gamma(\vec{q},{\rm Z})=\hbar q^4\frac{256\kappa_0^{3/2}}{9c_{\rm L}^3}C^{(3)}({\rm L})e^{-\hbar\omega(q,{\rm Z})/k_BT} \qquad (76)$$

The q^2 dependence in the classical regime has been predicted earlier[18].

From the study of $\Sigma^{(3)'}$ we find in the classical regime

$$\Sigma^{(3)'}(\vec{q},{\rm Z})=-\frac{32}{9c_{\rm L}}q^2\sqrt{\kappa_0}k_BTC^{(3)}({\rm L})ln\left(\frac{\omega_s({\rm L})}{\omega_l({\rm L})}\right), \qquad (77)$$

where $\omega_l({\rm L}){=}c_{\rm L}2\pi/l$ and $\omega_s({\rm L}){=}245$ THz. The phonon self-energy is negative and diverges logarithmically with the size of the system.

In the quantum regime the self-energy $\Sigma^{(3)'}(\vec{q},{\rm Z})$ vanishes exponentially with lowering T.

We next investigate the renormalization of the flexural mode due to fourth order anharmonicities. From Eqs. (23) and (25) we get

$$\Sigma^{(4)}(\vec{q},{\rm Z})=\frac{\hbar\omega(\vec{q},{\rm Z})}{N}\sum_{\vec{k},\lambda}\Phi^{(4)}\begin{pmatrix}{\rm Z}&\lambda&\lambda&{\rm Z}\\-\vec{q}&\vec{k}&-\vec{k}&\vec{q}\end{pmatrix}\Big[1{+}2n(\vec{k},\lambda)\Big], \qquad (78)$$

where λ={L, T, Z}. Separating in-plane and out of plane scattering modes λ we write

$$\Sigma^{(4)}(\vec{q},{\rm Z})=\Sigma^{(4)}(\vec{q},{\rm Z};\perp)+\Sigma^{(4)}(\vec{q},{\rm Z};{\rm Z}) \qquad (79)$$

where $\perp$ stands for {L, T}. We readily transform to frequency integrals and obtain

$$\Sigma^{(4)}(\vec{q},{\rm Z};\perp)=q^2\hbar\sum_\lambda C^{(4)}({\rm Z};\lambda)\int_{\omega_l(\lambda)}^{\omega_s(\lambda)}d\omega\,\omega^2\,\Big[1{+}2n(\omega)\Big], \qquad (80)$$

where for λ=L

$$C^{(4)}({\rm Z;L})=\frac{a^6\sqrt{3}(3n^{(4)}+p^{(4)})}{32\times 96\pi M_C^2c_{\rm L}^4}, \qquad (81)$$

while for λ=T, $n^{(4)}$ and $p^{(4)}$ are interchanged and $c_{\rm L}$ is replaced by $c_{\rm T}$. In Eq. (80) the integration limits are $\omega_s({\rm L})$=245 THz, $\omega_s({\rm T})$=151 THz, and for the sample with $l{=}10^4a$, $\omega_l({\rm L}){=}5.9{\times}10^{10}$ Hz, $\omega_l({\rm T}){=}3.65{\times}10^{10}$ Hz. In the classical case we have

$$\Sigma^{(4)}(\vec{q},{\rm Z};\perp)=q^2k_BT\sum_\lambda C^{(4)}({\rm Z};\lambda)\Big[\omega_s^2(\lambda)-\omega_l^2(\lambda)\Big] \qquad (82)$$

In the quantum regime zero point motion gives at $T=0$:

$$\Sigma^{(4)}(\vec{q},{\rm Z};\perp)=\frac{q^2\hbar}{3}\sum_\lambda C^{(4)}({\rm Z};\lambda)[\omega_s^3(\lambda)-\omega_l^3(\lambda)]. \qquad (83)$$

Likewise we obtain

$$\Sigma^{(4)}(\vec{q},{\rm Z};{\rm Z})=q^2\hbar C^{(4)}({\rm Z;Z})\int_{\omega_l({\rm Z})}^{\omega_s({\rm Z})}d\omega\;\;\Big[1+2n(\omega)\Big], \qquad (84)$$

where

$$C^{(4)}({\rm Z;Z})=\frac{a^6\sqrt{3}\;l^{(4)}}{16\times 96\pi M_C^2\kappa_0} \qquad (85)$$

with ω_s(Z)=94.25 THz and ω_l(Z)=4.25 MH
sical limit we get

$$\Sigma^{(4)}(\vec{q},\mathrm{Z};\mathrm{Z}) = 2q^2 k_B T C^{(4)}(\mathrm{Z};\mathrm{Z}) ln\left(\frac{\omega_s}{\omega_l}\right.$$

which diverges for an infinite system wh
Here zero point motion gives at T=0:

$$\Sigma^{(4)}(\vec{q},\mathrm{Z};\mathrm{Z}) = q^2 \hbar C^{(4)}(\mathrm{Z};\mathrm{Z})[\omega_s(\mathrm{Z}) - \omega_$$

From Eqs. (77), (80) and (82) we see th
butions to the flexural mode self-energy ar
and fourth order anharmonicities and are p
q^2 at long wavelengths. We then identify
in Eq. (32) as:

$$c_{\mathrm{Z}}^2 = \frac{\Sigma^{(3)'}(\vec{q},\mathrm{Z}) + \Sigma^{(4)}(\vec{q},\mathrm{Z})}{q^2}$$

Notice that the in-plane and out-of-pl
tions to $\Sigma'(\vec{q},\mathrm{Z})$ are proportional to q^2, as anticipated in Eq. (32). In the language of membrane theory[24] this result corresponds to a q^{-2} singularity due to the first anharmonic correction to the bare bending rigidity. We have evaluated expressions (77), (80) and (84) as function of temperature in the interval 0.1-2000 K. We find that the negative term $\Sigma^{(3)'}(\vec{q},\mathrm{Z})$ is more than two orders of magnitude smaller than the positive term $\Sigma^{(4)}(\vec{q},\mathrm{Z})$ and hence negligible. Both $\Sigma'(\vec{q},\mathrm{Z};\perp)$ and $\Sigma'(\vec{q},\mathrm{Z};\mathrm{Z})$ are monotone increasing functions with increasing T, with $\Sigma'(\vec{q},\mathrm{Z};\mathrm{Z}) > \Sigma'(\vec{q},\mathrm{Z};\perp)$. Above T=100 K, $\Sigma'(\vec{q},\mathrm{Z};\mathrm{Z})$ is more than one order of magnitude larger. In Fig. 6(a) we have plotted the sum $c_{\mathrm{Z}}^2 = \Sigma'(\vec{q},\mathrm{Z})/q^2$ for the case l=$10^4 a$. We find that for the case l=$10^2 a$ the renormalization effect is about a factor 2 smaller.

Finally we have studied the effect of renormalization on the thermal expansion. Therefore we have evaluated β_T(Z) by means of Eqs. (18) and (44), with $\omega(\vec{q},\mathrm{Z})$ replaced by the renormalized frequency $\Omega(\vec{q},\mathrm{Z})$, Eqs. (32) and (33). Thereby we take into account self-consistently that c_{Z}^2 depends on l and T. We obtain

$$\beta_T(\mathrm{Z}) = \frac{\tilde{\gamma}(\mathrm{Z})\hbar^2}{2\pi k_B T^2}\int_{q_l}^{q_s} dq\; q^3\; \frac{e^{\hbar\Omega(\vec{q},\mathrm{Z})/k_B T}}{\left(e^{\hbar\Omega(\vec{q},\mathrm{Z})/k_B T}-1\right)^2}, \quad (89)$$

where q_s=$(\omega_s(\mathrm{Z})/\sqrt{\kappa_0})^{1/2}$=$1.20\times10^8\mathrm{cm}^{-1}$ and q_l=$(\omega_l(\mathrm{Z})/\sqrt{\kappa_0})^{1/2}$=$2.56\times10^4\mathrm{cm}^{-1}$. In Fig. 6(b) we have plotted β_T(Z) as function of T. Notice that the renormalized β_T(Z) is in absolute value smaller than the unrenormalized quantity (empty squares). Hence the renormalization of the flexural mode favors the transition from negative to positive thermal expansion. The transition temperature T_α decreases with increasing size of the system. This is shown in Fig. 7, obtained by solving Eq. (56) self-consistently for the renormalized case. Although c_{Z}^2 diverges in the thermodynamic limit, the weak logarithmic divergence allows one in fact to consider systems of macroscopic size ($l = 10^8 a$).

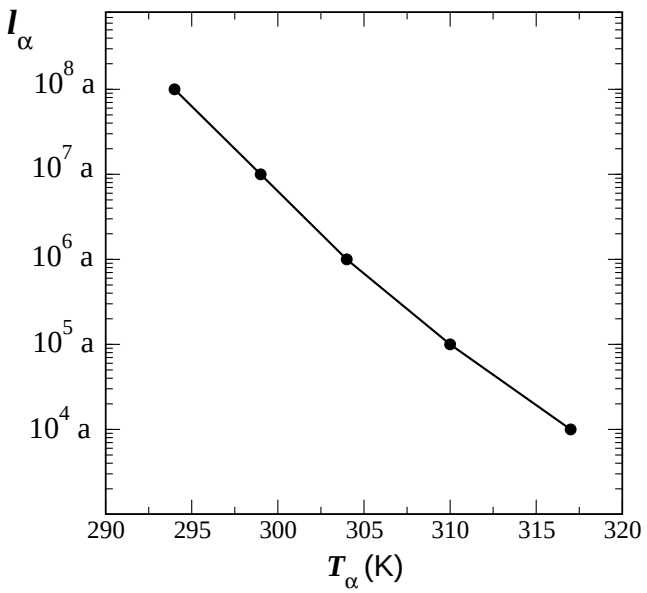

FIG. 7: System size l_α as function of temperature T_α for change from negative to positive thermal expansion. Discrete points are calculated self-consistently with renormalization of flexural mode.

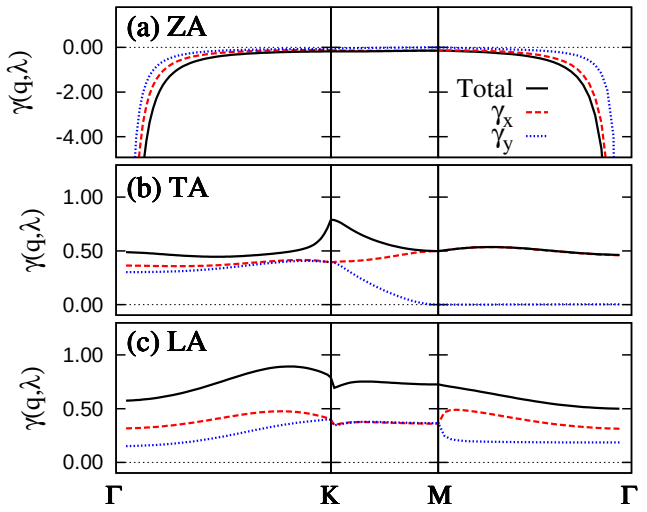

FIG. 8: (Color online) Generalized Grüneisen parameters $\gamma(\vec{q},\lambda)$ for (a) ZA, (b) TA and (c) LA acoustic phonon modes of graphene. $\gamma_x(\vec{q},\lambda)$ ($\gamma_y(\vec{q},\lambda)$), where x (y) refer to strain ϵ_{xx} (ϵ_{yy}), contribution is indicated by a dashed-red (dotted-blue) line.

For a recent discussion of the experimental situation, which includes analysis of substrate corrections, see Ref. 48.

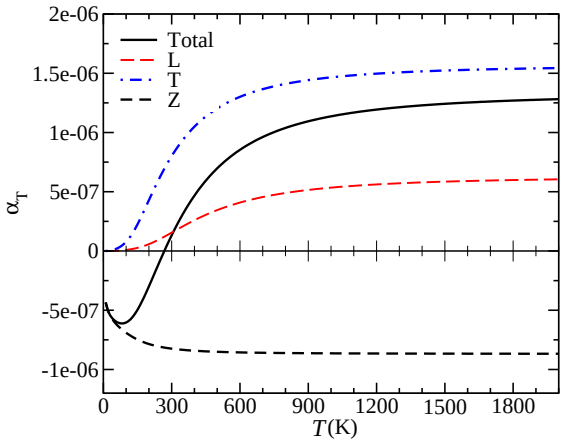

FIG. 9: (Color online) Temperature dependence of the thermal expansion coefficient α_T of graphene. Units K^{-1}. Sample size $l = 80a$.

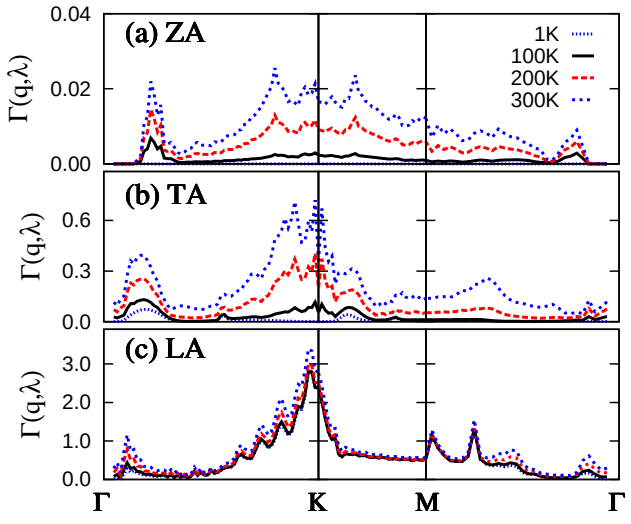

FIG. 10: (Color online) Temperature dependence of $\Gamma(\vec{q},\lambda)$ for (a) ZA, (b) TA and (c) LA acoustic phonon modes of graphene. Units cm^{-1}.

VII. NUMERICAL RESULTS

The physical quantities outlined above were calculated independently by numerical techniques. This approach serves for verifying the analytical predictions and for obtaining valid results in an extended range of temperatures and wave vectors. We investigate Umklapp-processes at the edges of the BZ. The calculation was realized through a discrete mesh of $\vec{q}$-points in the BZ which was designed following the description presented in Ref. 49. The basic steps of the algorithm are given in Appendix B.

The generalized Grüneisen parameters $\gamma(\vec{q},\lambda)$ (Eq. (20)) obtained for $\vec{q}$ along the Γ-K-M-Γ high symmetry crystallographic path are shown in Fig. 8. The results are to be compared with their analytical counterparts Eq. (44) for $\gamma(\vec{q},\,\mathrm{Z})$ and Eq. (48) for $\gamma(\perp)$. In particular in Eq. (44) we have shown that $\gamma(\vec{q},\,\mathrm{Z})$ is negative and diverges as q^{-2} in the thermodynamic limit. Notice that even in the case of a relatively dense mesh of $\vec{q}$-values we are limited in the numerical approach as will be discussed below. For the in-plane contributions $\gamma(\mathrm{T})$ and $\gamma(\mathrm{L})$, we find that both are positive and approach finite values, in agreement with Eq. (48).

The thermal expansion coefficient α_T (Eq. (17)), displayed in Fig. 9, behaves also as predicted (see Fig. 4). The flexural (in-plane) mode(s) contribution is negative (positive) in the whole range of T. However, here the crossover from negative to positive thermal expansion takes place at ≈ 275 K. This value is expected from the discrete mesh adopted in the calculation where the smallest values of $\vec{q}$ considered correspond to a system size $l \approx 80\ a$ (see Appendix B). Inclusion of smaller values of $\vec{q}$ (larger system sizes) is out of reach due to numerical inaccuracy in the diagonalization of the dynamical matrix. Notice that this result does not include the renormalization of the flexural mode discussed at the end of Sect. VI B.

We proceed now with the study of the frequency shifts and linewidths. In the previous analysis (Sect. VI) we restricted ourselves, for simplicity, to the most important scattering processes at low $\vec{q}$. The numerical treatment of the problem, nevertheless, allows a complete survey of every possible scattering mechanism. We start with the frequency linewidths which, using the same notation as before, can be calculated through:

$$\Gamma(\vec{q},\lambda) = \frac{\pi\hbar}{2N}\sum_{\vec{q}_2\vec{q}_3}\sum_{\lambda_2\lambda_3}\left|\Phi^{(3)}\begin{pmatrix}\lambda\lambda_2\lambda_3\\ -\vec{q}\vec{q}_2\vec{q}_3\end{pmatrix}\right|^2\Big\{\Big[1+n(\vec{q}_2,\lambda_2)+n(\vec{q}_3,\lambda_3)\Big]\delta\Big(\omega(\vec{q},\lambda)-\omega(\vec{q}_2,\lambda_2)-\omega(\vec{q}_3,\lambda_3)\Big)$$
$$+\,2\Big[n(\vec{q}_2,\lambda_2)-n(\vec{q}_3,\lambda_3)\Big]\delta\Big(\omega(\vec{q},\lambda)+\omega(\vec{q}_2,\lambda_2)-\omega(\vec{q}_3,\lambda_3)\Big)\Big\}. \qquad (90)$$

The δ-function was represented as $\delta(\omega) = \lim_{\xi\to 0} e^{-\omega^2/\xi^2}/(\xi\sqrt{\pi})$. After having analyzed a broad range of parameters we found good convergence in the results by adopting $\xi = 5$ cm^{-1} (see Appendix B). This value is comparable to the one used in related studies[19,49,50].

In Fig. 10 we show the total phonon linewidths $\Gamma(\vec{q},\lambda)$ obtained for the three acoustical modes λ=ZA, TA and LA, at different temperatures as indicated. Notice the different scales that have been adopted on the Γ-axes. This behaviour is a result of the larger possibilities for damping, satisfying conservation laws, available for LA, and then, subsequently for TA and ZA. Similar to what happens in normal 3D metals, such as Cu, Ag and Au, peaked structures located at intermediate values of $\vec{q}$ are present[51,52]. As we show below, they are associated with different active scattering channels. With the raise of temperature, higher phonon occupations in Eq. (90), produce an increase in the phonon linewidths due to the thermal activation of additional scattering processes for every value of $\vec{q}$.

The total linewidths, together with its contributions from Normal and Umklapp processes for T=1 and 300 K, are displayed in Fig. 11. Umklapp processes become comparable to Normal processes only near the border of the BZ, close to the K- and the M-point[53]. For the flexural phonon mode at T=1 K $\Gamma(\vec{q},$ Z) is null ($< 10^{-7}$) irrespective of the value of $\vec{q}$. Then at 300 K, $\Gamma(\vec{q},$ Z) is non zero in a large region of the Γ-K-M-Γ path but it still vanishes in the limit $q \to 0$. On the other hand, in-plane mode linewidths, $\Gamma(\vec{q},$ T) and $\Gamma(\vec{q},$ L), experience larger changes with T in the long wavelength regime. In this limit, they both vary about two orders of magnitude with increasing T from 1 to 300 K (from $\sim 10^{-3}$ to $\sim 10^{-1}$) and, as we discussed before, different behaviors for low- and high-T can be identified.

The relative importance of the scattering mechanisms is obtained by considering separately each of the summands in Eq. (90). The dependence with the wave vector $\vec{q}$ for all of the active scattering channels at T=1 and 300 K are shown in Fig. 12. Partial contributions to the linewidth of the flexural mode ZA are finite in a large sector of the Γ-K-M-Γ path only at 300 K (the case T=1 K is included to emphasize that $\Gamma(\vec{q},$ Z) is null). Here the main important active channels are ZA$\leftrightarrow$ZA-TA and ZA-LA (top right panels). It has been reported that processes where ZA phonons are present can exist only if two of them participate simultaneously in the scattering. This result, which has been referred as a selection rule[36,54], is verified by our findings.

The scattering of in-plane phonons presents more complicated characteristics than that of the flexural phonons discussed above. In this case a larger number of channels are already open at low-T. For the TA mode at T=1 K, the active scattering channels are TA$\leftrightarrow$ZA+ZA and TA+TA (middle left). Then, at 300 K, TA$\leftrightarrow$TA-LA, TA-TA and LA-LA become also activated by T and the relative dominance of each them depends strongly on $\vec{q}$ in a non trivial way (middle right). For the LA mode the picture is more complex. Due to its larger frequency, already at low-T, LA$\leftrightarrow$ZA+ZA, TA+TA, LA+LA and LA+TA are all active (bottom left). Then, at 300 K additionally LA$\leftrightarrow$LA-LA becomes important, particularly in the limit $q \to 0$ (bottom right).

The behaviour of the scattering channels in the long wavelength regime is analyzed in more detail in Fig. 13. In agreement with the analytical description, we observe that at low-T (T=1 K) the dominant scattering processes are TA$\leftrightarrow$ZA+ZA and LA$\leftrightarrow$ZA+ZA (left panels). At 300 K however, TA$\leftrightarrow$TA-TA and LA$\leftrightarrow$LA-LA become more important (right panels). Notice that while in the analytical approach presented before we were able to study larger system sizes ($l = 10^4\ a$) with the current numerical treatment we are limited to $l \approx 80\ a$. Therefore, in the long wavelength regime the results shown in Fig. 5 for the ZA+ZA scattering channel of in-plane phonon modes are complementary to those in Fig. 13. We remark the good agreement obtained between both independent calculations (see the values of q in the x-axis of both figures).

Further interesting insights on the features of the anharmonic scattering for the in-plane phonon modes are presented in Fig. 14. Here we show the spatial distribution inside the BZ for a few selected relevant scattering channels with $\vec{q}$ equal to $\vec{q}_A$, $\vec{q}_B$ and $\vec{q}_C$ (middle points of $\Gamma-$K$-$M$-\Gamma$) at 300 K. These curves can be interpreted as follows. The plot displayed on the top left panel describes the processes where an excited TA phonon, with fixed momentum $\vec{q} = \vec{q}_A$, is scattered through every possible $\vec{q}_2$ by the channel ZA+ZA (remember that $\vec{q}_3 = -\vec{q}_A - \vec{q}_2 \pm \vec{G}$). Notice that due to the conservation of energy and momentum only a reduced number of processes are active. The resulting circular shaped line (around $\vec{q}_A$) indicates that ZA phonons propagating in every possible direction will be generated from the original unperturbed in-plane TA $\vec{q}_A$ phonon. The blue-dashed line separates Normal (region enclosing $\vec{q}_A$) from Umklapp processes. Here the absence of Umklapp contributions is consistent with the result of Fig. 12 (middle-right panel) where the Umklapp TA$\leftrightarrow$ZA+ZA process vanishes for values of $\vec{q}$ right above $\vec{q}_A$.

Similar analysis can be performed for the remaining panels of Fig. 14. Observe in particular that for $\vec{q} = \vec{q}_B$, with $\vec{q}_B$ located at the border of the BZ, Umklapp processes become more important. Additional similar plots are presented in Appendix B. These results are relevant for the microscopical understanding of the thermal conductivity since they determine to which extent any excited phonon, in any given initial direction, will be scattered by phonons propagating in any other direction.

Finally, we study the 3rd- and 4th-order[55,56] frequency shifts which can be calculated through:

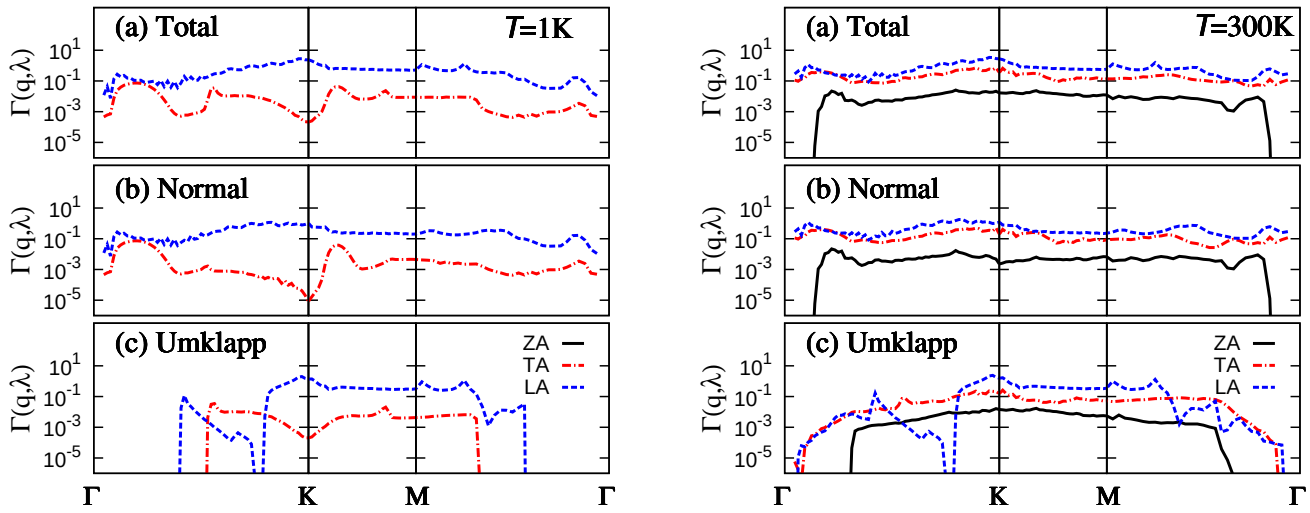

FIG. 11: (Color online) Phonon linewidths $\Gamma(\vec{q},\lambda)$ for T=1 (left) and 300 K (right). The log-scale for the y-axis is used to allow comparison of Normal and Umklapp contributions. Units cm^{-1}.

$$\Delta^{(3)}(\vec{q},\lambda)=\frac{\hbar}{2N}\sum_{\vec{q}_2\vec{q}_3}\sum_{\lambda_2\lambda_3}\left|\Phi^{(3)}\begin{pmatrix}\lambda\lambda_2\lambda_3\\-\vec{q}\vec{q}_2\vec{q}_3\end{pmatrix}\right|^2 P\Big\{\frac{1+n(\vec{q}_2,\lambda_2)+n(\vec{q}_3,\lambda_3)}{\omega(\vec{q},\lambda)-\omega(\vec{q}_2,\lambda_2)-\omega(\vec{q}_3,\lambda_3)}-\frac{1+n(\vec{q}_2,\lambda_2)+n(\vec{q}_3,\lambda_3)}{\omega(\vec{q},\lambda)+\omega(\vec{q}_2,\lambda_2)+\omega(\vec{q}_3,\lambda_3)}$$
$$+\frac{2[n(\vec{q}_2,\lambda_2)-n(\vec{q}_3,\lambda_3)]}{\omega(\vec{q},\lambda)+\omega(\vec{q}_2,\lambda_2)-\omega(\vec{q}_3,\lambda_3)}\Big\}, \tag{91}$$

$$\Delta^{(4)}(\vec{q},\lambda)=\frac{\hbar}{2N}\sum_{\vec{q}_1,\lambda_1}\Phi^{(4)}\begin{pmatrix}\lambda\lambda_1\lambda_1\lambda\\-\vec{q}\vec{q}_1-\vec{q}_1\vec{q}\end{pmatrix}\Big[1+2n(\vec{q}_1,\lambda_1)\Big]. \tag{92}$$

In this case the principal part P was represented as $P\{1/\omega\}=\omega/(\omega^2+\eta^2)$ with $\eta=1$ cm^{-1} (Appendix B).

The obtained results are displayed in Fig. 15. In agreement with the analytical prediction, the 3rd-order frequency shift of the flexural ZA mode is negative and experiences a logarithmic divergence in the long wavelength regime. In this limit, for the in-plane modes on the contrary, $\Delta^{(3)}(\vec{q}$,T) tends to zero with almost no appreciable variation versus T and $\Delta^{(3)}(\vec{q}$, L) is negligibly small at low-T but it increases smoothly with T.

The strong 3rd-order negative bandshift $\Delta^{(3)}(\vec{q}$, Z) near Γ means, in principle, that another configuration different from a flat sample, will be more stable. As we show in Fig. 15 (right), 4th-order anharmonic interactions counterbalances the 3rd-order bandshift, at $\vec{q}\to 0$, for the ZA mode and stabilize the layer. Other characteristics in this regime are the linear dependence with $\vec{q}$ of $\Delta^{(4)}(\vec{q}$,T) and $\Delta^{(4)}(\vec{q}$,L) which are in agreement with the conclusions derived in Eq. (72).

VIII. CONCLUSIONS

We have studied thermal expansion and phonon broadenings and lineshifts of non-ionic 2D crystals by means of anharmonic lattice dynamics, thereby implementing analytical and numerical methods. We have used a semi-empirical model for the interatomic force constants, comprising in-plane acoustic phonons and out-of-plane flexural modes.

Analytical techniques allow to investigate the long wavelength limit which is beyond the reach of numerical calculations and ab-initio methods. Since the out-of-plane Grüneisen constant γ(Z) diverges logarithmically in the $\vec{q}\to 0$ limit, we have considered crystals of finite size and investigated finite size effects. We have taken graphene as an example for quantitative evaluations. Thereby we have found a change of sign of the thermal expansion as a function of crystal size. A change of sign has been found earlier by Monte Carlo calcula-

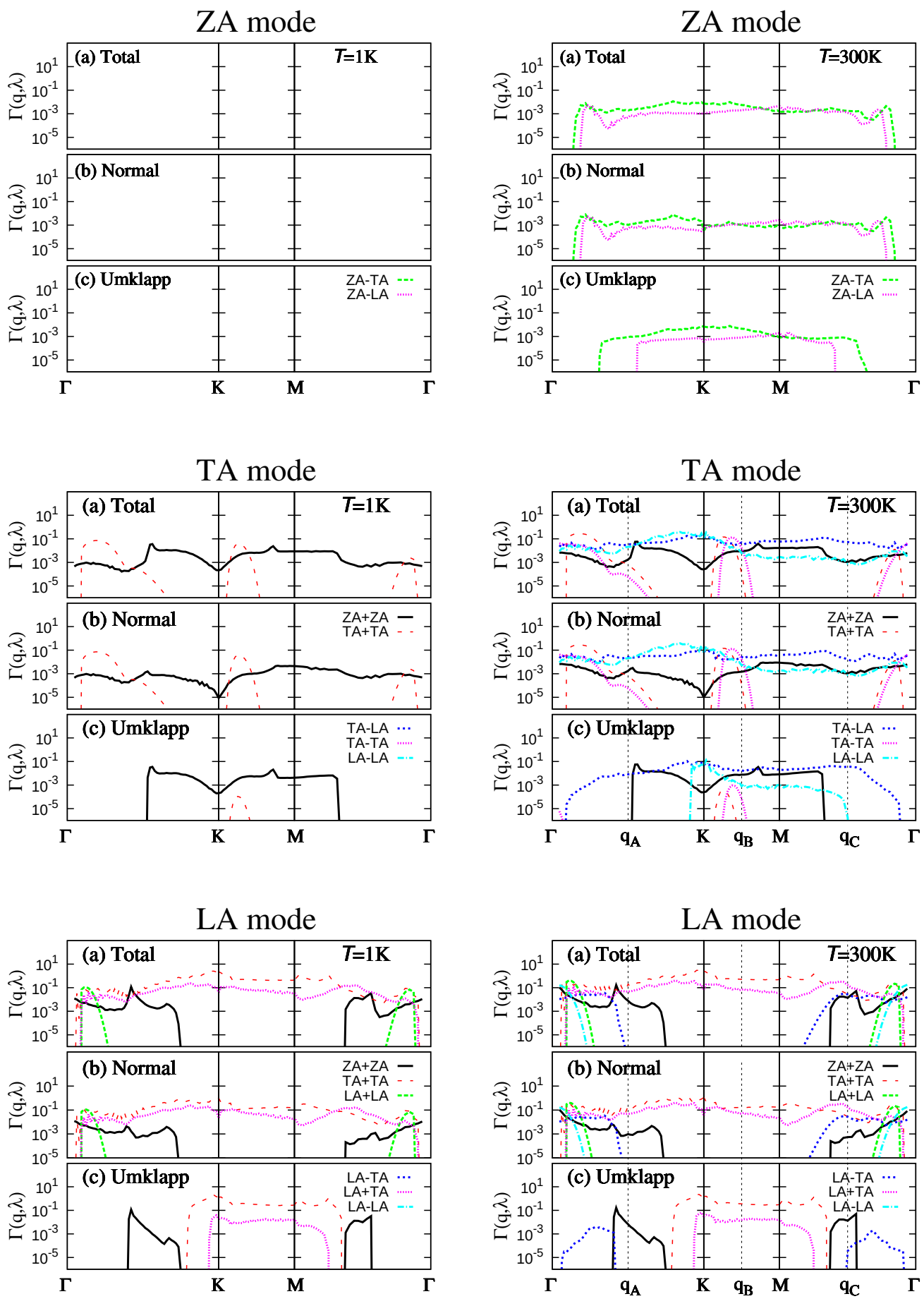

FIG. 12: (Color online) Contribution of the different scattering channels to the phonon linewidths at T=1 K (left) and 300 K (right). The total linewidth (a) is composed of Normal (b) and Umklapp (c) processes. Units cm^{-1}.

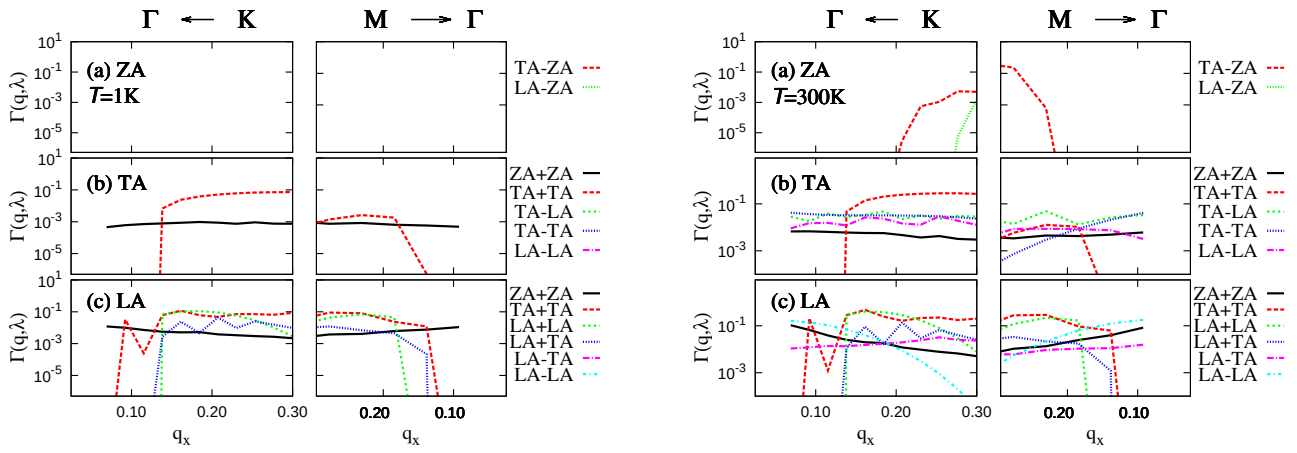

FIG. 13: (Color online) Contribution of the different scattering channels to the phonon linewidths at 1 K (left panels) and 300 K (right panels) in the long wavelength regime. Units cm^{-1} (q_x (x-axis) is given in units of $\mathring{A}^{-1}$).

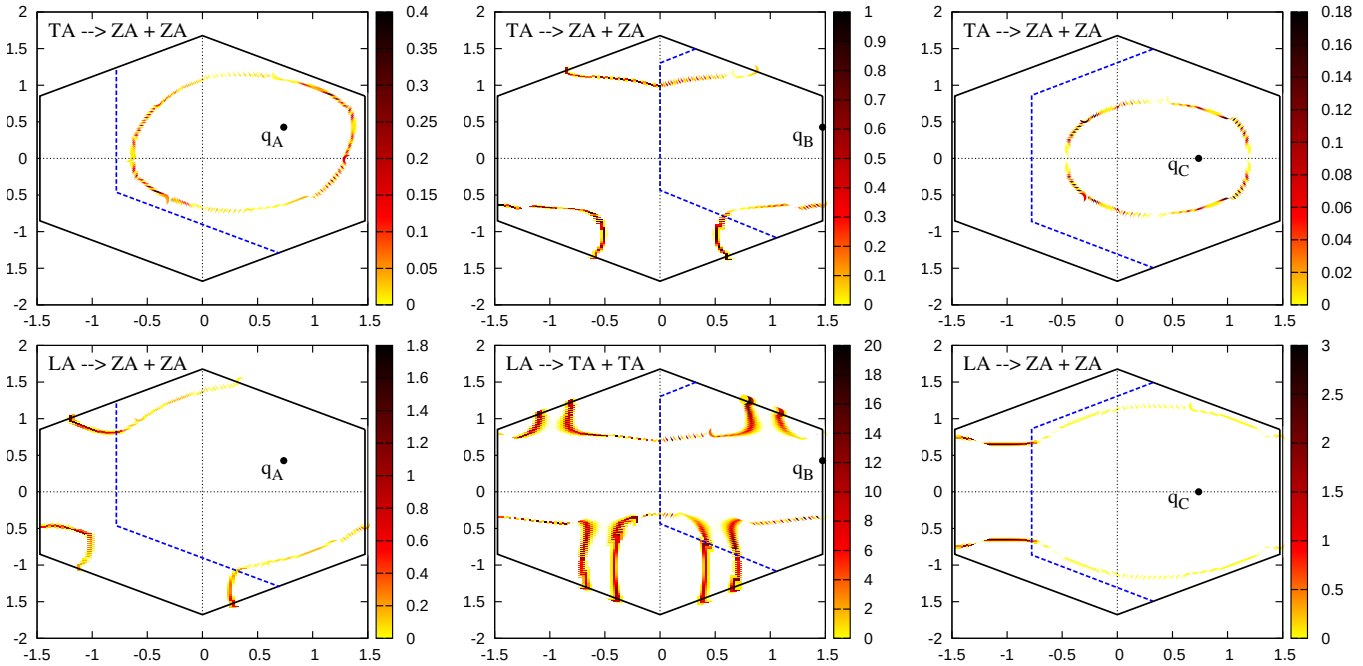

FIG. 14: (Color online) Contour plots of the contribution of selected scattering channels inside the BZ for the TA and LA acoustic phonon modes of graphene at $\vec{q}_A, \vec{q}_B$ and $\vec{q}_C$ (i. e. the middle points of Γ−K−M−Γ). Units cm^{-1} (q_x (x-axis) and q_y (y-axis) are given in units of $\mathring{A}^{-1}$).

tions[15], there the finite size of the system is inherent in the method.

We have investigated analytically the wave vector dependence of the decays and lineshifts of in-plane and out-of-plane phonons in the classical (high T) and in the quantum regime. In the classical regime we confirm earlier results about the decay rates of an in-plane phonon into two flexural modes and of the inverse absorption process[18]. In the quantum regime the wave vector dependence and the T dependence of these processes are different. We have studied the lineshifts (equivalently the real part of the self energy) due to third and fourth order anharmonicities. In the classical regime the real part of the self energy of the flexural mode in a third order absorption process is found to be negative, proportional to T and q^2, and diverging logarithmically with the size of the system. In the quantum regime it vanishes exponentially with decreasing T. Self energy corrections of the flexural mode due to fourth order anharmonic processes are positive and proportional to q^2 in the classical as well as in the quantum regime. Similar results have been obtained for crystalline membranes in the classical[24] and in

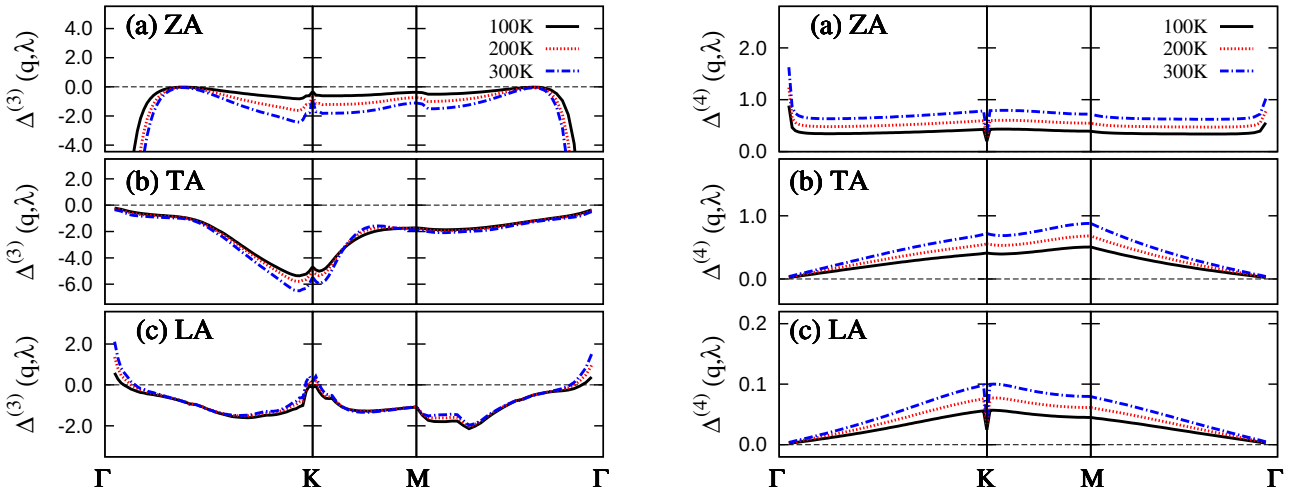

FIG. 15: (Color online) Temperature dependence of the 3rd- (left panel) and 4th-order (right panel) bandshifts for the (a) ZA, (b) TA and (c) LA acoustic phonon modes of graphene. Units cm^{-1}.

the quantum[20] regimes. As a consequence of the corresponding change of the dispersion of the flexural mode at long wavelengths[20,42], we find that the temperature T_α of the change from negative to positive thermal expansion is lowered and close to 300 K for systems of macroscopic size.

The numerical analysis (Sect. VII and Appendix B) is complementary to the analytical treatment of Sect. VI. Special care has been devoted to obtain a dense grid of $\vec{q}$ points covering the BZ. Various scattering channels that contribute to decays and lineshifts of the in-plane and out-of-plane modes have been investigated in a systematic way. In the nearest numerically attainable neighborhood of the Γ-point we find agreement between analytical and numerical results. In addition, beyond the long wavelength regime, we have studied Umklapp processes and compared their contributions with Normal processes for various scattering channels. We find that in a broad T range below room temperature the decay rate of flexural modes is much less affected by Umklapp processes than the decay rate of in-plane modes. This result supports earlier theoretical conclusions that flexural modes are responsible for an anomalous large intrinsic thermal conductivity[18,19,29,30,57].

Acknowledgments

We thank B. Verberck, D. Lamoen and A. Dobry for useful comments. We acknowledge funding from the FWO (Belgium)-MINCyT (Argentina) collaborative research project. This work is supported by the Euro GRAPHENE project CONGRAN.

Appendix A

We calculate the change of the phonon frequency $\omega(\vec{q},\lambda)$ under homogeneous strains ϵ_{ij} $(i,j \in \{1,2\})$ in two dimensions for a non primitive crystal. Homogeneous strains are related to the center of mass displacement of the unit cell $\vec{n}$ by

$$s_i(\vec{n}) = \sum_j \epsilon_{ij} X_j^s(\vec{n}), \tag{A-1}$$

where the center of mass equilibrium position reads

$$\vec{X}^s(\vec{n}) = \sum_\kappa \frac{M_\kappa}{M} X_j(\vec{n}\kappa), \tag{A-2}$$

and where $M = \sum_\kappa M_\kappa$ is the total mass per unit cell. Hence

$$s_i(\vec{n}) = \sum_\kappa u_i(\vec{n}\kappa), \tag{A-3}$$

with

$$u_i(\vec{n}\kappa) = \sum_j \epsilon_{ij} \frac{M_\kappa}{M} X_j(\vec{n}\kappa). \tag{A-4}$$

We need to calculate

$$\delta\omega(\vec{q},\lambda) = \sum_i \frac{\partial\omega(\vec{q},\lambda)}{\partial X_i(\vec{n}\kappa)} u_i(\vec{n}\kappa), \tag{A-5}$$

where $u_i(\vec{n}\kappa)$ is given by Eq. (A-4). Starting from Eq. (7) we obtain

$$\delta\omega(\vec{q},\lambda) = \frac{1}{2\omega(\vec{q},\lambda)} \sum_{kl} \sum_{\kappa_1\kappa_2} \frac{e_k^{\kappa_1 *}(\vec{q},\lambda) e_l^{\kappa_2}(\vec{q},\lambda)}{\sqrt{M_{\kappa_1} M_{\kappa_2}}} \times \sum_{\vec{h}_2} \delta\Phi_{kl}^{(2)}(\vec{0}\kappa_1; \vec{h}\kappa_2) e^{i\vec{q}[\vec{X}(\vec{h}\kappa_2) - \vec{X}(\vec{0}\kappa_1)]}. \tag{A-6}$$

The change of the second order coupling parameter due to the displacements $u_i(\vec{n}\kappa)$ reads

$$\delta\Phi^{(2)}_{kl}(\vec{0}\kappa_1;\vec{h}\kappa_2)=\sum_{\vec{n}\kappa i}\Phi^{(3)}_{kli}(\vec{0}\kappa_1;\vec{h}\kappa_2;\vec{n}\kappa)u_i(\vec{n}\kappa), \quad \text{(A-7)}$$

where $\Phi^{(3)}$ is the third order anharmonic coupling.

Differentiation of Eq. (A-6) with respect to the strains yields

$$\frac{\partial\omega(\vec{q},\lambda)}{\partial\epsilon_{ij}}=\frac{1}{2\omega(\vec{q},\lambda)}\sum_{kl}\sum_{\kappa_1\kappa_2\kappa}\sum_{\vec{n}\vec{h}}\frac{e^{\kappa_1 *}_k(\vec{q},\lambda)e^{\kappa_2}_l(\vec{q},\lambda)}{\sqrt{M_{\kappa_1}M_{\kappa_2}}}\Phi^{(3)}_{kli}(\vec{0}\kappa_1;\vec{h}\kappa_2;\vec{n}\kappa)X_i(\vec{n}\kappa)\frac{M_\kappa}{M}e^{i\vec{q}[\vec{X}(\vec{h}\kappa_2)-\vec{X}(\vec{0}\kappa_1)]} \quad \text{(A-8)}$$

For the case of central forces we obtain

$$\frac{\partial\omega(\vec{q},\lambda)}{\partial\epsilon_{ii}}=-\frac{1}{4\omega(\vec{q},\lambda)M_C}\sum_{kl}\sum_{\kappa\kappa'}\sum_{\vec{n}}\varphi^{(3)}_{kli}(\vec{0}\kappa;\vec{n}\kappa')\Big[X_i(\vec{n}\kappa')-X_i(\vec{0}\kappa)\Big]$$
$$\times\Big[e^{\kappa *}_k(\vec{q},\lambda)e^{\kappa'}_l(\vec{q},\lambda)-e^{\kappa' *}_k(\vec{q},\lambda)e^{\kappa}_l(\vec{q},\lambda)e^{i\vec{q}.[\vec{X}(\vec{n}\kappa')-\vec{X}(\vec{0}\kappa)]}\Big] \quad \text{(A-9)}$$

Using $\varphi^{(3)}_{kli}(\vec{0}\kappa;\vec{n}\kappa')=-\varphi^{(3)}_{kli}(\vec{n}\kappa';\vec{0}\kappa)$ we see that the right hand side of (A-9) is symmetric with respect to an interchange of atoms $(\vec{n}\kappa')\leftrightarrow(\vec{0}\kappa)$. In case of graphene, acoustic modes satisfy $e^A_k(\vec{q},\lambda)=e^B_k(\vec{q},\lambda)$.

Appendix B

Anharmonic force constants $\Phi^{(3)}\binom{\lambda_1\lambda_2\lambda_3}{\vec{q}_1\vec{q}_2\vec{q}_3}$ (Eq. (10)) and $\Phi^{(4)}\binom{\lambda_1\lambda_2\lambda_3\lambda_4}{\vec{q}_1\vec{q}_2\vec{q}_3\vec{q}_4}$ (Eq. (14)) are defined by Fourier transforms given by rather complex summations where each term contains multiple factors such as the energy $\omega(\vec{q},\lambda)$ and the polarization vector $e^\kappa_i(\vec{q},\lambda)$ evaluated at distinct values of $\vec{q}$ and λ simultaneously. The first step in the construction of an algorithm is therefore to obtain and store $\omega(\vec{q},\lambda)$ and $e^\kappa_i(\vec{q},\lambda)$ for the $\vec{q}$-points which will be included in the calculation.

This first step was done here by using a code developed previously for the study of harmonic phonons in graphene reported in Ref. 35. Due to the symmetry of the crystal, numerical diagonalization of the dynamical matrix $D(\vec{q})$, carried out through packages from the LAPACK libraries[58], is performed only inside the irreducible part (IP) of the Brillouin zone (1BZ) (Fig B-1 (left)). Further phonon frequencies and polarization vectors, on the remaining $\vec{q}$-points in the entire 1BZ, are generated by symmetry operations satisfying the properties $\vec{e}(\vec{q},\lambda)=\vec{e}^*(-\vec{q},\lambda)$ and $\omega(\vec{q},\lambda)=\omega(-\vec{q},\lambda)$, as well as the orthonormality and closure conditions:

$$\sum_{\kappa i}e^{\kappa *}_i(\vec{q},\lambda)e^\kappa_i(\vec{q},\lambda')=\delta_{\lambda\lambda'}, \quad \text{(B-1a)}$$

$$\sum_{\lambda}e^{\kappa *}_i(\vec{q},\lambda)e^{\kappa'}_j(\vec{q},\lambda)=\delta_{ij}\delta_{\kappa\kappa'}. \quad \text{(B-1b)}$$

Because of the band-crossing as function of the phonon momentum $\vec{q}$, the use of an auxiliary algorithm, based on the eigenvector orthogonality, is needed to maintain the sorting of phonon modes after diagonalization[59].

Momentum conservation in Eq. (12) implies that $\vec{q_1}$, $\vec{q_2}$ and $\vec{q_3}$ included in the calculation must satisfy

$$\vec{q_1}+\vec{q_2}+\vec{q_3}=\pm\vec{G}, \quad \text{(B-2)}$$

where $\vec{G}$ is a vector of the reciprocal lattice. For this purpose we adopted a special finite mesh in such a way that $\vec{q_1}$, $\vec{q_2}$ and $\vec{q_3}$, satisfying Eq. (B-2), belong to the mesh itself what reduces considerably the number of diagonalizations of the dynamical matrix. The mesh is defined such that every $\vec{q}$-point is given by

$$\vec{q}=n_1\vec{\delta}_1+n_2\vec{\delta}_2 \quad \text{(B-3)}$$

where n_1 and n_2 are integers and $\vec{\delta}_1$ and $\vec{\delta}_2$ are the unit vectors that define the mesh. The algorithm was designed following closely the steps described in Ref. 49 where anharmonicities of surface phonons in Al were studied[60]. We refer the reader to that work for further details on the construction of the mesh.

Convergence of numerical results was verified by comparing results for three different meshes with 81, 225 and 729 distinct $\vec{q}$-points inside the IP. Figure B-1 (left) displays the case with 225 $\vec{q}$-points. A comparison of the different meshes near the Γ point is displayed in Fig. B-1 (right). Note that smaller meshes are subsequently contained in the larger ones. Thus, by increasing the mesh we keep the existing $\vec{q}$-points and new ones, lying at the intermediate distance between two consecutive wave-vectors, are added.

Contributions from Normal and Umklapp processes are identified in a simple way. Given a fixed $\vec{q}_1$, the summation over $\vec{q}_2$ in Eqs. (90) and (91) runs over the whole BZ. For each pair $\vec{q}_1$, $\vec{q}_2$, $\vec{q}_3$ becomes unambiguously defined by $\vec{q}_3=-\vec{q}_1-\vec{q}_2$. Then, if the wave-vector $\vec{q}_3$ lies inside the BZ the process is Normal. Otherwise, a non-zero $\pm G$

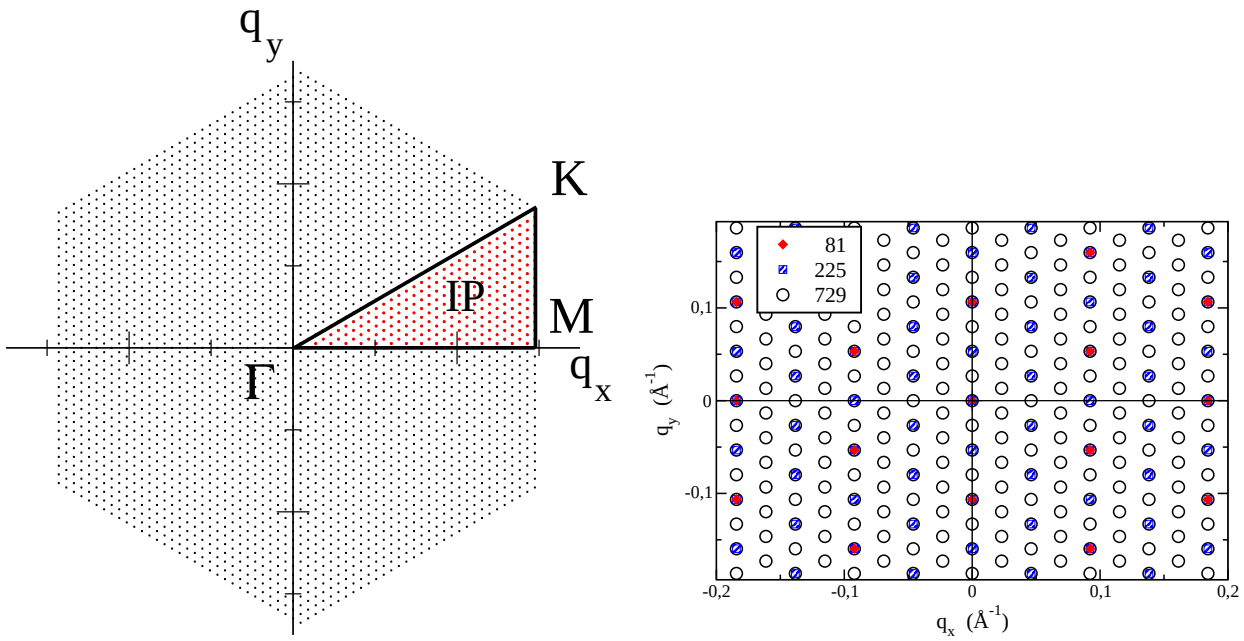

FIG. B-1: Discrete mesh with 225 $\vec{q}$-points inside the irreducible part (IP) of the 1BZ (left). Comparison of meshes in the vicinity of the Γ-point (right).

is used to re-map $\vec{q}_3$ to its equivalent $\vec{q}$-point inside the BZ and the process is counted as Umklapp.

The dependence of the numerical results for the 3rd-order linewidths $\Gamma(\omega, \vec{q})$ and bandshifths $\Delta(\omega, \vec{q})$ with the number of $\vec{q}$-points of the mesh at T=100 K is analyzed in Fig. B-2. The overall agreement as function of the phonon momentum is evident. Similar results were found also for other temperatures. The total number of individual scattering processes, for every possible scattering channel, considered in the whole path Γ-K-M-Γ for each mesh is shown in Table B-1.

Mesh	Normal	Umklapp
729	922594	621662
225	118407	77689
81	15581	9697

TABLE B-1: Total number of scattering processes included in the calculation for the whole high-symmetry crystallographic path Γ-K-M-Γ.

The auxiliar variables ξ and η required to evaluate the δ-function and the principal part P, respectively, are studied on Fig. B-3. Here we show the case of 729 $\vec{q}$-points inside the IP at T=100 K. As is expected, when ξ is too small the phonon linewidths $\Gamma(\vec{q}, \lambda)$ results in uncorrelated peaks, i. e. $\xi = 0.1$ cm^{-1} (solid-red curve). In the opposite limit, i. e., $\xi = 20$ cm^{-1} (dot-dashed light-blue curve), the peaks become over-broadened and the phonon linewidth is over-estimated. Therefore we used $\xi = 5$ cm^{-1} (solid black curve), which results in good convergence and is consistent with values adopted in previous related studies[19,49,50]. Similar trend is present with the behavior of η. In this case the best choice turned out to be $\xi = 1$ cm^{-1}.

A last point which deserves special mention is the determination of the scattering channels. This point constitutes a mayor test for the accurancy of the code. Given a particular $\vec{q}$, any scattering process

$$\begin{aligned} \lambda_1 &\leftrightarrow \lambda_2 + \lambda_3 \\ (\lambda_1 &\leftrightarrow \lambda_2 - \lambda_3) \end{aligned} \tag{B-4}$$

should be identically to

$$\begin{aligned} \lambda_1 &\leftrightarrow \lambda_3 + \lambda_2 \\ (\lambda_1 &\leftrightarrow \lambda_3 - \lambda_2). \end{aligned} \tag{B-5}$$

for arbitrary λ_i= ZA, TA and LA, with $i = 1, 2, 3$. These processes, however, are calculated independently and the equality is valid only after the complete summations (Eqs. (90) and (91)) over the entire BZ (every possible $\vec{q}_2$ is included) are performed. Thus, every single process involving different $\vec{q}_1$, $\vec{q}_2$ (and $\vec{q}_3$) has to be taken into account properly, otherwise the equivalence will not be satisfied.

The relationships (B-5) and (B-6) can be viewed as a consequence of the symmetry of the lattice and the properties of the inter-atomic force constants under interchange of $\vec{q}_2$ with $\vec{q}_3$. Note for instance that using the

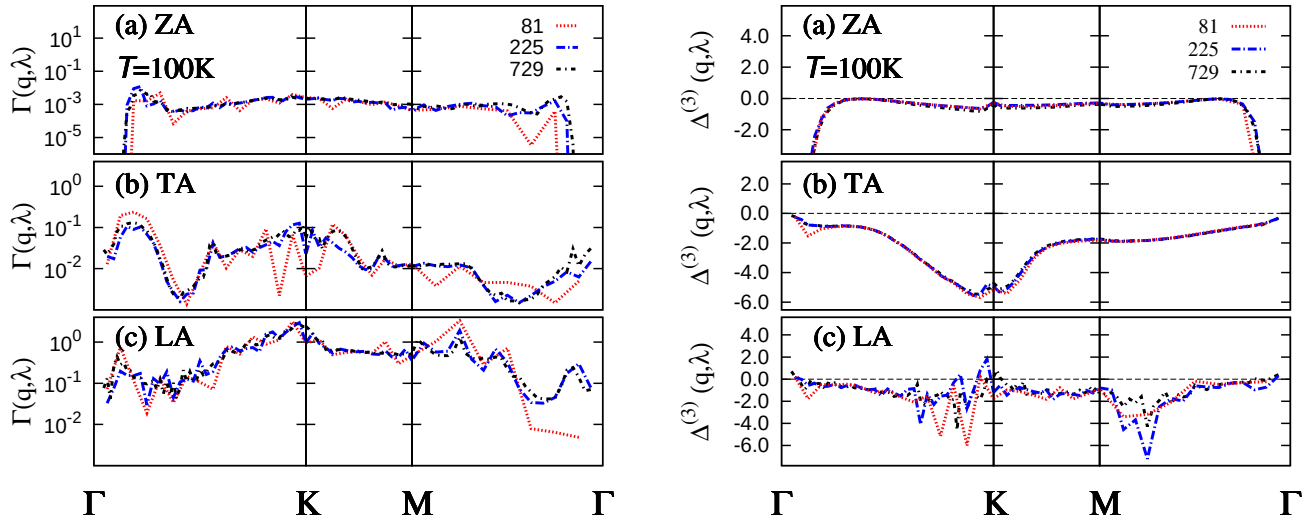

FIG. B-2: (Color online) Comparison of results for the linewidth (left panels) and phonon shift (right panels) for different number of q-points in the mesh along the BZ.

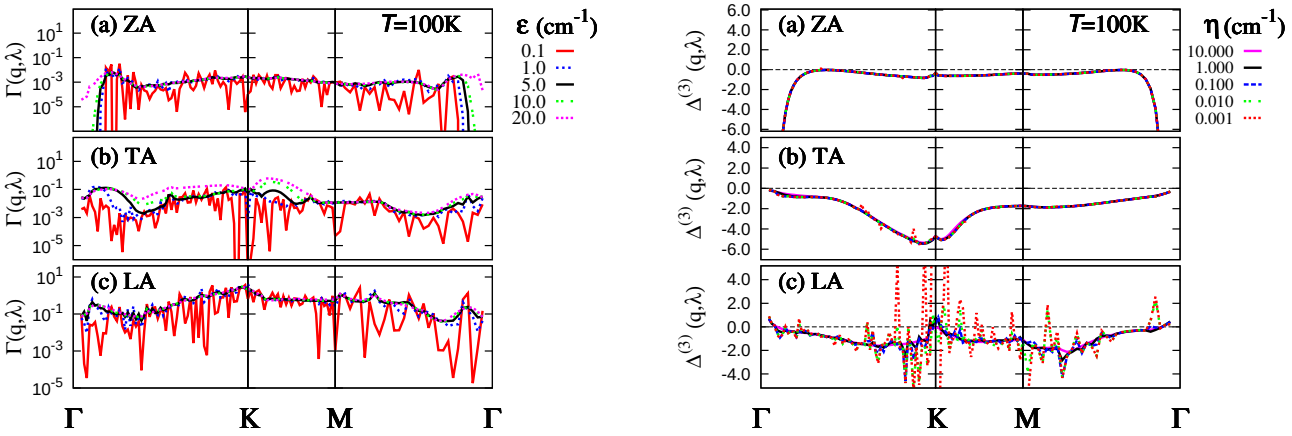

FIG. B-3: (Color online) Effects of the auxiliar variables η and ϵ on the evaluation of the principal part and the delta function in the calculation of the phonon shift (right panels) and linewidths (left panels).

equations of the Sect. IV, it can be shown that

$$\Phi^{(3)}_{ijk}\begin{pmatrix} BBB \\ \vec{q}_1\vec{q}_2\vec{q}_3 \end{pmatrix} = \Phi^{(3)}_{ijk}\begin{pmatrix} BBB \\ \vec{q}_1\vec{q}_3\vec{q}_2 \end{pmatrix}. \tag{B-6}$$

The same is valid for $\Phi^{(3)}_{ijk}\left(\begin{smallmatrix} AAB \\ \vec{q}_1\vec{q}_2\vec{q}_3 \end{smallmatrix}\right)$, $\Phi^{(3)}_{ijk}\left(\begin{smallmatrix} AAA \\ \vec{q}_1\vec{q}_2\vec{q}_3 \end{smallmatrix}\right)$ and $\Phi^{(3)}_{ijk}\left(\begin{smallmatrix} BAA \\ \vec{q}_1\vec{q}_2\vec{q}_3 \end{smallmatrix}\right)$. The remaining anharmonic force constant satisfy instead the following conditions where, in addition to $\vec{q}_2$ and $\vec{q}_3$, the order of the A and B atoms must be also interchanged

$$\Phi^{(3)}_{ijk}\begin{pmatrix} BAB \\ \vec{q}_1\vec{q}_2\vec{q}_3 \end{pmatrix} = \Phi^{(3)}_{ijk}\begin{pmatrix} BBA \\ \vec{q}_1\vec{q}_3\vec{q}_2 \end{pmatrix} \tag{B-7}$$

$$\Phi^{(3)}_{ijk}\begin{pmatrix} ABA \\ \vec{q}_1\vec{q}_2\vec{q}_3 \end{pmatrix} = \Phi^{(3)}_{ijk}\begin{pmatrix} AAB \\ \vec{q}_1\vec{q}_3\vec{q}_2 \end{pmatrix} \tag{B-8}$$

$$\Phi^{(3)}_{ijk}\begin{pmatrix} AAB \\ \vec{q}_1\vec{q}_2\vec{q}_3 \end{pmatrix} = \Phi^{(3)}_{ijk}\begin{pmatrix} ABA \\ \vec{q}_1\vec{q}_3\vec{q}_2 \end{pmatrix} \tag{B-9}$$

$$\Phi^{(3)}_{ijk}\begin{pmatrix} AAB \\ \vec{q}_1\vec{q}_2\vec{q}_3 \end{pmatrix} = \Phi^{(3)}_{ijk}\begin{pmatrix} ABA \\ \vec{q}_1\vec{q}_3\vec{q}_2 \end{pmatrix}. \tag{B-10}$$

With the replacement of expressions in Eqs. (B-6) to (B-10) into the Eq. (91) for $\Phi^{(3)}\left(\begin{smallmatrix} \lambda_1\lambda_2\lambda_3 \\ \vec{q}_1\vec{q}_2\vec{q}_3 \end{smallmatrix}\right)$ together with

the interchange of λ_2 and λ_3 it can be shown that

$$\Phi^{(3)}_{AAA}\begin{pmatrix}\lambda_1\lambda_2\lambda_3\\ \vec{q}_1\vec{q}_2\vec{q}_3\end{pmatrix} = \Phi^{(3)}_{AAA}\begin{pmatrix}\lambda_1\lambda_3\lambda_2\\ \vec{q}_1\vec{q}_2\vec{q}_3\end{pmatrix} \quad \text{(B-11)}$$

$$\Phi^{(3)}_{ABB}\begin{pmatrix}\lambda_1\lambda_2\lambda_3\\ \vec{q}_1\vec{q}_2\vec{q}_3\end{pmatrix} = \Phi^{(3)}_{ABB}\begin{pmatrix}\lambda_1\lambda_3\lambda_2\\ \vec{q}_1\vec{q}_2\vec{q}_3\end{pmatrix} \quad \text{(B-12)}$$

$$\Phi^{(3)}_{BBB}\begin{pmatrix}\lambda_1\lambda_2\lambda_3\\ \vec{q}_1\vec{q}_2\vec{q}_3\end{pmatrix} = \Phi^{(3)}_{BBB}\begin{pmatrix}\lambda_1\lambda_3\lambda_2\\ \vec{q}_1\vec{q}_2\vec{q}_3\end{pmatrix} \quad \text{(B-13)}$$

$$\Phi^{(3)}_{BAA}\begin{pmatrix}\lambda_1\lambda_2\lambda_3\\ \vec{q}_1\vec{q}_2\vec{q}_3\end{pmatrix} = \Phi^{(3)}_{BAA}\begin{pmatrix}\lambda_1\lambda_3\lambda_2\\ \vec{q}_1\vec{q}_2\vec{q}_3\end{pmatrix} \quad \text{(B-14)}$$

and, for example, that

$$\Phi^{(3)}_{BBA}\begin{pmatrix}\lambda_1\lambda_2\lambda_1\\ \vec{q}_1\vec{q}_2\vec{q}_3\end{pmatrix} = \Phi^{(3)}_{BAB}\begin{pmatrix}\lambda_1\lambda_1\lambda_2\\ \vec{q}_1\vec{q}_2\vec{q}_3\end{pmatrix} \quad \text{(B-15)}$$

$$\Phi^{(3)}_{AAB}\begin{pmatrix}\lambda_1\lambda_2\lambda_3\\ \vec{q}_1\vec{q}_2\vec{q}_3\end{pmatrix} = \Phi^{(3)}_{ABA}\begin{pmatrix}\lambda_1\lambda_2\lambda_1\\ \vec{q}_1\vec{q}_2\vec{q}_3\end{pmatrix} \quad \text{(B-16)}$$

and other similar ones, where we have used the notation

$$\Phi^{(3)}_{\kappa_1\kappa_2\kappa_3}\begin{pmatrix}\lambda_1\lambda_2\lambda_1\\ \vec{q}_1\vec{q}_2\vec{q}_3\end{pmatrix} = \frac{e_i^{\kappa_1}(\vec{q}_1,\lambda_1)e_i^{\kappa_2}(\vec{q}_2,\lambda_2)e_i^{\kappa_3}(\vec{q}_3,\lambda_3)}{\sqrt{8\omega(\vec{q}_1,\lambda_1)\omega(\vec{q}_2,\lambda_2)\omega(\vec{q}_3,\lambda_3)}} \times\Phi^{(3)}_{iii}\begin{pmatrix}\kappa_1\kappa_2\kappa_3\\ \vec{q}_1\vec{q}_2\vec{q}_3\end{pmatrix}. \quad \text{(B-17)}$$

In addition, the calculation of any given $\Phi^{(3)}_{ijk}$ requires the evaluation of exponential functions where the scalar product $\vec{q}\cdot\vec{X}$ may result in an integer fraction of π. Any small error or loss of precision in the sum over the wave vectors $\vec{q}_1$, $\vec{q}_2$, $\vec{q}_3$ (Normal) and $\pm\vec{G}$ (Umklapp) can prevent the numerical equivalence between Eqs. (B-5) and (B-6).

Finally, the spatial distribution inside the BZ of the scattering channels (Fig. B-4) is also representative of the accurancy of the code (this figure is complementary to Fig. 14). Notice therein the perfect match of the blue dotted line between Normal and Umklapp contributions which, as we explained above, require the inclusion of a reciprocal lattice vector $\vec{G}$.

* Electronic address: karl.michel@uantwerpen.be
† Electronic address: costamagna@ifir-conicet.gov.ar
‡ Electronic address: francois.peeters@uantwerpen.be

[1] J. M. Ziman, *Electrons and Phonons: The theory of Transport Phenomena in Solids*, Oxford University Press, Oxford (1960).
[2] See e.g., A. A. Maradudin, *Dynamical Properties of Solids*, Vols. 1 and 2, G. K. Horton and A. A. Maradudin Eds., North-Holland Publ. Co, Amsterdam (1974).
[3] K. S. Novoselov, A.K. Geim, S. V. Morosov, D. Jiang, Y. Zhang, S. V. Dubonos, I.V. Grigorieva, and A. A. Frisov, Science **306**, 666 (2004).
[4] K. S. Novoselov, D. Jiang, F. Schedin, T. J. Booth, V. V. Khotkevich, S. V. Morozov, and A. K. Geim, Science **102**, 10451 (2005).
[5] A. H. Castro Neto, F. Guinea, N. M. R. Peres, K. S. Novoselov, and A. K. Geim, Reviews of Modern Physics **81**, 109 (2009).
[6] J. C. Meyer, A. K. Geim, M. I. Katsnelson, K. S: Novoselov, D. Obergfell, S. Roth, C. Girit, and A. Zette, Nature (London) **446**, 60 (2007).
[7] D. Yoon, Y-W. Son, and H. Cheong, Nano Letters **11**, 3227 (2011).
[8] W. Bao, F. Miao, Z. Chen, H. Zhang, W. Janoy, C. Dames, and C. N. Lau, Nat. Nanotechnol. **4**, 562 (2009).
[9] A. A. Balandin, S. Ghosh, W. Bao, I. Calizo, D. Teweldebrhan, F. Miao, and C. N. Lau, Nano Lett. **8**, 902 (2008).
[10] H. Seol, I. Jo, A. L. Moore, L. Lindsay, Z. H. Aitken, M. T. Pettes, X. Li, Z. Yao, R. Huang, D. Broido, N. Mingo, R. S. Ruoff, and L. Shi, Science **328**, 213 (2010).
[11] Z. Wang, R. Xie, C. T. Bui, D. Liu, X. Ni, B. Li, and J. T. L. Long, Nano Lett. **11**, 112 (2011).
[12] A. A. Balandin, Nature Materials **10**, 569 (2011).
[13] I. M. Lifshitz. Zh. Eksp. Teor. Fiz. **22**, 475 (1952).
[14] N. Mounet and N. Marzari, Phys. Rev. B **71**, 205214 (2005).
[15] K. V. Zakharchenko, M. I. Katsnelson, and A. Fasolino, Phys. Rev. Lett. **102**, 046808 (2009).
[16] A. L. C. da Silva, L. Candido, J. N. Teisceira Rabelo, G. Q. Hai, and F. M. Peeters, EPL **107**, 56004 (2014).
[17] A. Fasolino, J. H. Los, and M. I. Katsnelson, Nat. Mater. **6**, 858 (2007).
[18] N. Bonini, J. Garg, and N. Marzari, Nano Lett. **12**, 2673 (2012).
[19] L. Paulatto, F. Mauri, and M. Lazzeri, Phys. Rev. B **87**, 214303 (2013).
[20] B. Amorin, R. Roldan, E. Cappellutti, A. Fasolino, F. Guinea and M. I. Katnelson, Phys. Rev. B **89**, 224307 (2014).
[21] P. M. Chaikin and T. C. Lubensky, *Principles of condensed matter physics*, Cambridge University Press, Cambridge (1995).
[22] D. Nelson, T. Piran and S. Weinberg, *Statistical Mechanics of Membranes and Surface*, Word Scientic, Singapore (1989).
[23] L. D. Landau and E. M. Lifshitz, *Elastizitätstheorie* (Akademie-Verlag, Berlin, 1968).
[24] D. R. Nelson and L. Peliti, J. Physique **48**, 1085 (1987).
[25] M. Mohr, J. Maultzsch, E. Dobardzie, S. Reich, I. Milosevic, M. Damnjanovic, A. Bosak, M. Krisch, and C. Thom-

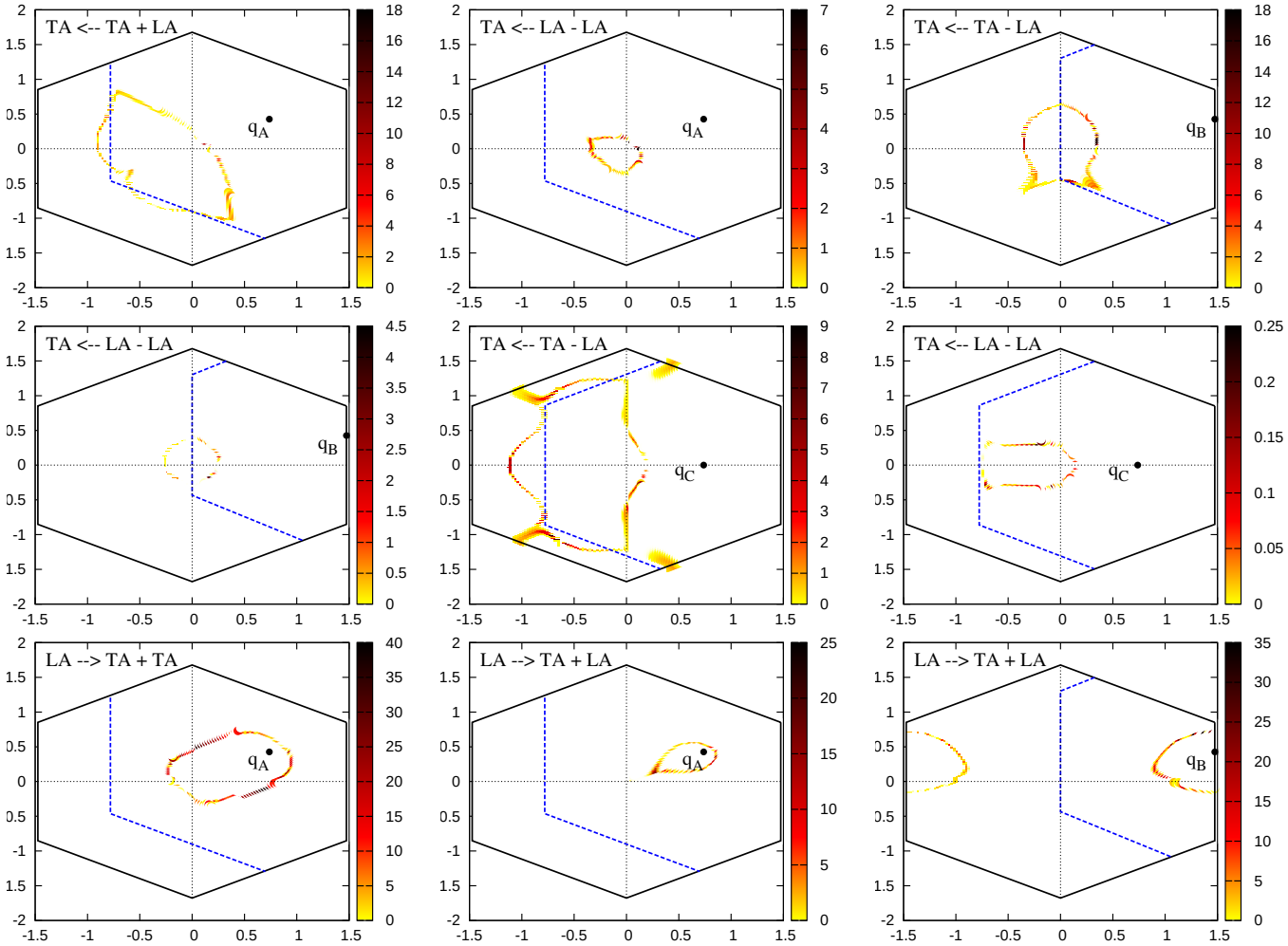

FIG. B-4: (Color online) Contour plots of the contribution of selected scattering channels along the BZ for the TA and LA acoustic phonon modes of graphene at $\vec{q}_A, \vec{q}_B$ and $\vec{q}_C$ (i. e. the middle points of $\Gamma-K-M-\Gamma$). Units cm^{-1} (q_x (x-axis) and q_y (y-axis) are given in units of $\AA^{-1}$).

sen, Phys. Rev. B **76**, 035439 (2007).

[26] D. L. Nika, A. S. Askerov, and A. A. Balandin, Nano Letters **12**, 3238 (2012).

[27] D. L. Nika and A. A. Balandin, J. Phys.: Condens. Matter **24** 233203 (2012).

[28] T. Feng and X. Ruan, Journal of Nanomaterials **2014**, 206370 (2014).

[29] L. Lindsay, D. A. Broido, and N. Mingo, Phys. Rev. B **82**, 115427 (2010).

[30] D. Singh, J. Y. Murthy, and T. S. Fisher, J. Appl. Phys. **110**, 094312 (2011).

[31] M. Born and K. Huang, *Dynamical Theory of Crystal Lattices*, (Oxford University Press, New York, 1952).

[32] R. Saito, G. Dresselhaus, and M. S. Dresselhaus, *Physical Properties of Carbon Nanotubes* (Imperial College, London, 1998).

[33] S. Reich, C. Thomson, and J. Maultzsch, *Carbon Nanotubes* (Wiley-VCH, Weinheim, 2004).

[34] R. Peierls, *Quantum theory of Solids*, (Oxford) 1955.

[35] K. H. Michel and B. Verberck, Phys. Rev. B **78**, 085424 (2008).

[36] L. Lindsay, D. A. Broido, and N. Mingo, Phys. Rev. B **80**, 125407 (2009).

[37] R. Nicklow, N. Wakabayashi, and H. G. Smith, Phys. Rev. B **5**, 4951 (1971).

[38] G. Leibfried and W. Ludwig, *Theory of Anharmonic Effects in Crystals*, Solid State Physics vol. **12**, edited by F. Seitz and D. Turnbull (Academic press, New York, 1661).

[39] W. Götze and K. H. Michel, Phys. Rev. **157**, 738 (1967).

[40] J. Kokkedee, Physica **28**, 374 (1962).

[41] A. A. Maradudin and A. E. Fein, Phys. Rev. **128**, 2589 (1962).

[42] E. Mariani and F. von Oppen, Phys. Rev Lett. **100**, 076801 (2010).

[43] P. Scuracchio, S. Costamagna, F. M. Peeters, and A. Dobry, Phys. Rev. B **90**, 035429 (2014).

[44] M. Hanfland, H. Beister, and K. Syassen, Phys. Rev. B **39**, 12598 (1989).

[45] T. M. G. Mohiuddin, A. Lombardo, R. R. Nair, A. Bonetti, G. Savini, R. Golil, N. Bonini, D. M. Basko, C. Galiotis, N. Marzari, K,. S. Novoselov, A. K. Geim and, A. C. Ferrari, Phys. Rev. B **79**, 205433 (2009).

[46] L. D. Landau and E. M. Lifshitz, *Statistische Physik*, Teil 1, Akademie-Verlag, Berlin (1987).
[47] C. Sevik, Phys. Rev. B **89** 035422 (2014).
[48] S. Linas, Y. Magnin, B. Poinsot, O. Boisron, G. D. Forster, Z. Han, D. Kalita, V. Bouchiat, V. Martinez, R. Fulcrand, F. Tournus, V. Dupuis, F. Rabilloud, L. Bardotti, F. Calvo, preprint arXiv:1411.7840v1 (2014).
[49] F. Franchini, G. Santoro, V. Bortolani, A. A. Maradudin, and R. F. Willis, Phys. Rev. B **45**, 11982 (1992).
[50] A. Greco, S. Koval, and R. Migoni, J. Phys.: Condens. Matter **4**, 5291 (1992).
[51] X. Tang, C. L. Li, and B. Fultz, Phys. Rev. B **82**, 184301(2010).
[52] X. Tang and B. Fultz, Phys. Rev. B **84**, 054303 (2011).
[53] D. L. Nika, E. P. Pokatilov, A. S. Askerov, and A. A. Balandin, Phys. Rev. B **79**, 155413 (2009).
[54] L. Lindsay, D. A. Broido, and N. Mingo, Phys. Rev. B **82**, 115427 (2010).
[55] E. Haro, M. Balkanski, R. F. Wallis, and K. H. Wanser, Phys. Rev. B **34**, 5358 (1986).
[56] E. Haro-Poniatowski, J. L. Escamilla-Reyes, and K. H. Wanser, Phys. Rev. B **53**, 12121 (1996).
[57] D. Singh, J. Y. Murthy, and T. S. Fisher, J. Appl. Phys. **110**, 044317 (2011).
[58] http://www.netlib.org/lapack
[59] L. F. Huang and Z. Zeng, J. Appl. Phys. **113**, 083524 (2013).
[60] M. Zoli, G. Santoro, V. Bortolani, A. A. Maradudin, and R. F. Willis, Phys. Rev. B **41**, 7507 (1990).